DOI: https://doi.org/10.2138/am-2019-6516

Revision 1

In situ measurements of lead and other trace elements in abyssal peridotite sulfides

Megan E. D'Errico[1], Matthew A. Coble[2] and Jessica M. Warren[3*]

[1]School of Science and Technology, Sonoma State University, Rohnert Park, CA 94928, USA; derrico@sonoma.edu
[2]Department of Geological Sciences, Stanford University, Stanford, CA 94305, USA; coblem@stanford.edu
[3]Department of Geological Sciences, University of Delaware, Newark, DE 19716, USA; warrenj@udel.edu
[*] Corresponding author

Key words: mantle; Pb; SIMS; sulfide; peridotite

Length: Main text= 11,442 words; Abstract= 328 words; Tables= 4; Figures= 11
Supplemental Material: Methods= 1,687 words; Tables= 4; Figures= 2 sets

Submitted to: *American Mineralogist*, special issue on *Planetary Processes as Revealed by Sulfides and Chalcophile Elements* on February 20th, 2018

Revisions submitted: *American Mineralogist*, special issue on *Planetary Processes as Revealed by Sulfides and Chalcophile Elements* on October 8th, 2018

This is a preprint, the final version is subject to change, of the American Mineralogist (MSA)
Cite as Authors (Year) Title. American Mineralogist, in press.
DOI: https://doi.org/10.2138/am-2019-6516

ABSTRACT

In the mantle, base metal sulfides have been proposed as the main host for many chalcophile and siderophile elements. This includes elements such as Pb, Se, and Te, which are often used as tracers of processes ranging from planetary accretion to mantle melting. We present *in situ* measurements of these elements, along with As, Sb, Ag, Au, and Cl, in abyssal peridotite sulfides to provide constraints on the storage of these elements in the mantle. A total of 152 sulfides from 11 peridotites and 1 pyroxenite from the Gakkel and Southwest Indian ridges were analyzed. The sulfides are pentlandites, some of which contain either discrete chalcopyrite domains or Cu-rich intergrowths. Trace element concentrations in 108 unaltered sulfides range from 2 to 36 ppm Pb, 45 to 250 ppm Se, <4 to 360 ppm Te, <1.5 to 1900 ppm As, 2 to 420 ppm Sb, 2 to 340 ppm Ag, 2 to 770 ppb Au, and 0.2 to 1000 ppm Cl. Tellurium abundances are highly variable within sulfides, which is likely due to the presence of telluride micro- or nano-phases. Based on morphology, composition, and the absence of monosulfide solid solution, the sulfides are interpreted to have formed by fractional crystallization from sulfide melt during conductive cooling of the mantle beneath the ridge axis. The average sulfide Pb concentration of 4 ppm can be reproduced by >90% fractional crystallization from a sulfide melt. The remaining sulfide melt, which is modeled to contain 800 ppm Pb, will dissolve into silicate melt as it rises through the mantle due to the increasing solubility of sulfur in silicate melt as pressure decreases. However, the amount of sulfide melt that remains after fractional crystallization is too low (mode of <0.005%) to contribute a significant amount of Pb to mid-ocean ridge basalts. We conclude that sulfides are not the main host for mantle Pb, even prior to the onset of any melting, and that the majority of mantle Pb is stored in silicate phases.

This is a preprint, the final version is subject to change, of the American Mineralogist (MSA)
Cite as Authors (Year) Title. American Mineralogist, in press.
DOI: https://doi.org/10.2138/am-2019-6516

INTRODUCTION

Peridotites, which are direct samples of the upper mantle, provide fundamental information regarding the chemical differentiation and evolution of the Earth. One of the most useful tracers of these processes is lead (Pb), as it is the daughter product of radiogenic decay of U and Th, both of which have long half-lives suitable for tracing processes at the million- to billion-year timescales. As a chalcophile element, Pb readily combines with sulfur (e.g., Shimazaki and MacLean, 1976; Kiseeva and Wood, 2013; Lorand and Luguet, 2016) and base metal sulfides have been proposed as a major control on the behavior of Pb in the upper mantle (e.g., Meijer et al., 1990; Hart and Gaetani, 2006). The control of sulfide, particularly sulfide melts, on Pb behavior is indicated by the partition coefficients (D) between monosulfide solid solution (MSS; the main sulfide phase in the upper mantle), sulfide melt and silicate melt. For example, $D_{Pb}^{\text{MSS/sulfide melt}}$ is 0.005 and $D_{Pb}^{\text{sulfide melt/basalt}}$ is 17, whereas $D_{Pb}^{\text{MSS/basalt}}$ is 0.2 at 1200°C and 1.5 GPa (Brenan, 2015). These observations suggest that mantle sulfides are key for understanding the transport, long-term storage, and abundance of mantle Pb.

Despite the affinity of Pb to partition into sulfide phases and the implications for the mantle Pb budget, the amount of Pb contained in sulfides has not been extensively studied. In peridotites, Fe-Ni-Cu base metal sulfides are found at trace levels (<0.02% modal abundances; Luguet et al., 2001, 2003). Meijer et al. (1990) proposed that sulfides are the main host of mantle Pb based on the mass balance comparison of Pb in bulk peridotites compared to Pb in olivine, orthopyroxene and clinopyroxene. Using the Meijer et al. (1990) measurements, Hart and Gaetani (2006) proposed that upper mantle sulfides contain 75 ppm Pb prior to mantle melting, based on predicted whole rock Pb contents and an estimated sulfide modal abundance of 0.05% in the source mantle. Early direct measurements of Pb in sulfides focused on inclusions in

This is a preprint, the final version is subject to change, of the American Mineralogist (MSA)
Cite as Authors (Year) Title. American Mineralogist, in press.
DOI: https://doi.org/10.2138/am-2019-6516

diamonds (Eldridge et al., 1991; Rudnick et al., 1993; Bulanova et al., 1996) and found an average of 171 ppm Pb in MSS sulfides from peridotitic diamonds. However, this may not be representative of typical convecting upper mantle due to the involvement of C-O-H fluids in their formation (e.g., Shirey and Shigley, 2013).

Previous analyses of sulfides from abyssal peridotites, seafloor samples collected at mid-ocean ridges, identified a range of 0.1–12 ppm Pb in 19 sulfides from 10 Gakkel and Southwest Indian Ridge (SWIR) samples (Warren and Shirey, 2012). A range of 2–8 ppm Pb was determined in 8 sulfides from one Mid-Atlantic Ridge (MAR) sample (Burton et al., 2012). Measurements in these studies were performed by single-grain dissolution and Pb extraction, which gives precise data but is a time-consuming technique, making analysis of many grains difficult and obscuring any intra-grain heterogeneity. More analyses of sulfide Pb contents are needed to improve constraints on the mass balance of Pb in peridotites and to aid in reconstructing Pb behavior during mantle melting.

In addition to Pb, sulfides are important hosts for other chalcophile and siderophile elements in the mantle, often controlling mantle budgets of these elements (e.g., Lorand and Luguet, 2016). Sulfides are the main host for mantle Os (e.g., Alard et al., 2000; Luguet et al., 2003; Harvey et al., 2011) and sulfide Re-Os isotopic compositions have been used to provide constraints on the timing of diamond formation (e.g., Pearson and Shirey, 1999; Pearson et al., 2007). Terrestrial mantle Se and Te concentrations have traditionally been used to constrain primitive mantle composition and trace early Earth accretion (e.g., Wang and Becker, 2013), though studies have also shown that the systematics of these elements may largely reflect melt extraction and refertilization (Lorand and Alard, 2010; König et al., 2014, 2015; Brenan, 2015). Many previous studies on siderophile and chalcophile elements in the mantle have been based on

This is a preprint, the final version is subject to change, of the American Mineralogist (MSA)
Cite as Authors (Year) Title. American Mineralogist, in press.
DOI: https://doi.org/10.2138/am-2019-6516

bulk rock analysis (e.g., Jagoutz et al., 1979; Morgan et al., 1981, 2001; Walker, 2016). However, several studies have focused on measurement of siderophile and chalcophile elements in peridotite-hosted sulfides (e.g., Lorand and Alard, 2001, 2010; Luguet et al., 2001; Harvey et al., 2006; Burton et al., 2012; Warren and Shirey, 2012; König et al., 2014).

To better constrain the amount of Pb and other elements (Se, Te, As, Sb, Ag, Au, and Cl) in peridotite sulfides, we performed *in situ* measurements of trace element concentrations using the sensitive high-resolution ion microprobe with reverse geometry (SHRIMP-RG). Previous *in situ* studies have examined trace elements in sulfides by ion microprobe (Eldridge et al., 1991; Rudnick et al., 1993), proton microprobe (Bulanova et al., 1996; Guo et al., 1999) and more recently by laser ablation inductively coupled plasma mass spectrometry (LA-ICPMS; Alard et al., 2000; Hayden et al., 2011; Lorand and Alard, 2001, 2010; Luguet et al., 2001; Norman et al., 2003; Wang et al., 2018). We used the SHRIMP-RG to measure trace elements in 150 sulfide grains from abyssal peridotites from the Gakkel Ridge and SWIR. *In situ* measurement of Pb and other trace elements by a relatively rapid technique allows us to establish a baseline trace element dataset for abyssal peridotite sulfides, which we then use to assess the behavior of sulfide-hosted elements during mantle melting and refertilization.

SAMPLES

Samples were selected from the Gakkel and SWIR dredge collections at Woods Hole Oceanographic Institution with the aim of analyzing peridotites to characterize both within- and between-dredge sulfide variability. For this study, sulfides were analyzed from 11 samples, of which seven are from the Gakkel Ridge and four are from the SWIR. Sample dredge locations

and lithologies are listed in Table 1. Silicate major and trace element compositions are discussed by Warren et al. (2009) for SWIR and D'Errico et al. (2016) for Gakkel.

For the Gakkel Ridge, we surveyed 203 large thin sections from 31 dredges and ranked samples according to their abundance of sulfides. Out of these samples, 67 were classified as containing "abundant" sulfides, 72 had sparse sulfides and the remaining 64 had no visible sulfide grains. The classification of sulfides as being abundant is a relative term used to indicate samples containing >3 analyzable sulfides (i.e., one or more grains of >100 μm diameter), whereas samples with sparse sulfides contain only one or two grains and were generally too small to analyze. Sulfide modes among all samples surveyed are assumed to be similar to the range of 0.001-0.06% reported for Kane Fracture Zone abyssal peridotites (Luguet et al., 2003), which was determined by point counting up to seven thin sections per sample.

Only samples rated as containing abundant sulfides were chosen for analysis and further sample selection was based on samples having a low degree of serpentinization and enough material available. Samples with abundant sulfides often contain evidence for interaction with silicate melt, suggesting that their higher sulfide abundances are due to interaction with melts. Data are thus biased toward samples that have undergone melt-rock interaction, a limitation of working on trace mineral phases, particularly when a dredged sample is small.

Gakkel peridotites in this study consist of five lherzolites and two harzburgites from the sparsely magmatic (SMZ) and eastern volcanic (EVZ) zones (Michael et al., 2003). In the SMZ, peridotites are relatively abundant and the oceanic crust is thin, whereas peridotites in the EVZ are less abundant and the crust is thicker, though still thinner than normal ocean crust (Jokat et al., 2003; Michael et al., 2003). Modes and major and trace elements for silicate minerals in the Gakkel samples are reported in D'Errico et al. (2016), except for sample HLY0102-70-62, which

is reported in Hellebrand et al. (2005). In addition, Warren and Shirey (2012) analyzed Pb and Re-Os isotopes in sulfides from some of these samples. In this study, we focus in detail on three samples from dredge PS59-235 in the SMZ, which contains fertile lherzolites with abundant sulfides (Table 1). In addition, we analyzed a typical lherzolite (PS59-238-75) and a refractory harzburgite with trapped melt (PS59-201-39) from the SMZ. For the EVZ, we analyzed one lherzolite (HLY0102-70-75) and one harzburgite (HLY0102-70-62) from the same dredge. The harzburgite contains sulfides that have very unradiogenic Pb and Re-Os isotope ratios compared to other Gakkel sulfides (Warren and Shirey, 2012).

SWIR samples were selected from a subset that had been analyzed for pyroxene and sulfide Pb, Re-Os, Rb-Sr and Sm-Nd isotopic compositions, along with silicate modes and major and trace elements (Warren et al., 2009; Warren and Shirey, 2012; Blusztajn et al., 2014). These samples are all from the ultraslow spreading Oblique Segment at 9-16°E (Dick et al., 2003; Standish et al., 2008). Two dredges were analyzed: dredge Van7-85, which was collected from an avolcanic section of the segment, and dredge Van7-96, from the inside corner high of the Oblique Segment with the Shaka Transform Fault. From dredge Van7-85, we analyzed two lherzolites (Van7-85-47 and -49) with typical modal and trace element abundances compared to other abyssal lherzolites (e.g., Warren, 2016). Dredge Van7-96 consists of lherzolites and harzburgites with pyroxenite veins, which display significant variations in Pb isotopes (Warren et al., 2009; Blusztajn et al., 2014). In Van7-96-21, we analyzed sulfides in the matrix (labeled M) and in the pyroxenite vein (labeled V). For comparison, we also analyzed an unveined lherzolite, Van7-96-28, which Warren et al. (2009) identified as having enriched Nd and Sr isotopic compositions similar to the veined peridotites. All samples from this dredge are

interpreted to have interacted with a melt generated during passage of Bouvet hotspot along the Shaka Fracture Zone around 15 Ma (Warren et al., 2009).

ANALYTICAL METHODS

For ion microprobe and scanning electron microscope (SEM) analyses, samples were mounted in 1" epoxy rounds. Pieces were either cut from polished thin sections or from polished rock slabs, as indicated in Table 1. Samples were examined with a reflected light microscope to identify sulfides that were large enough (>20 μm) to be analyzed. The petrography of each sulfide was documented prior to analysis using transmitted and reflected light photomicrographs to record sulfide size, distribution, morphology, and associated silicate minerals. Completely altered sulfides, identified by low reflectivity in reflected light, were avoided.

Energy dispersive spectroscopy (EDS) maps and secondary electron images of the sulfides and their host phases were collected using an Oxford Instruments X-Max 20 mm^2 silicon drift detector attached to a FEI Quanta 200 SEM located in the Department of Plant Biology at Carnegie Institution. This SEM has a W filament and was operated at an accelerating voltage of 15 kV and a spot size of 7 (which provides a measure of the relative beam current). The full emission spectrum was recorded for each map, from which the distribution of major and minor elements (Cu, Fe, Ni, Co, Zn, S) was used to assess compositional heterogeneity in the sulfides. Additional secondary and back-scattered electron images of the sulfide grains were taken using the JSM 5600 JEOL SEM at Stanford University.

Sulfide major element analyses by electron microprobe

This is a preprint, the final version is subject to change, of the American Mineralogist (MSA)
Cite as Authors (Year) Title. American Mineralogist, in press.
DOI: https://doi.org/10.2138/am-2019-6516

Major element compositions of sulfides were determined by Electron Microprobe Analysis (EMPA) at Stanford University, using a JEOL JXA-8230 SuperProbe equipped with five wavelength dispersive spectrometers. Details of the analytical setup are given in the Supplemental Methods. Sulfide analyses are reported as averages on a grain basis in Table 2 and the standard deviations for these averages in Table S2. In the case of sulfides that are partly altered, these appear in multiple categories in Table 2, with points from either the unaltered or altered portions used for averages depending on the category.

Pb analyses in sulfide by SHRIMP-RG with the O_2^- source

Lead concentrations in abyssal peridotite sulfides were determined using the SHRIMP-RG, which is co-operated by the U.S. Geological Survey and Stanford University. Trace elements were measured during three separate analytical sessions (denoted D1 to D3 in Table 1), details of which are given in the Supplemental Methods. Secondary ions were sputtered from a ~30 μm diameter spot using a 4–6 nA O_2^- primary beam for session D1. For the subsequent two sessions (D2, D3), the spot size was reduced to 20 μm, with a decreased primary beam current of 2–3 nA on the sample. Before every analysis, the sample surface was cleaned by rastering the primary beam in an area 45 μm x 45 μm around the analytical spot for 90–120 s. The acquisition table included $^{64}S_2^+$, $^{110}Fe_2^+$, $^{118}Ni_2^+$, $^{168}Fe_3^+$, $^{200}Fe_3O_2^+$, $^{206}Pb^+$ and $^{208}Pb^+$. Iron and Ni isotopes were used as guide and centering peaks. For Pb, mass 208 was measured for 40 s and mass 206 for 60 s. All other masses were measured for 1–5 s. The Pb background was determined by counting for 30 s at ~0.1 AMU above the ^{208}Pb peak (i.e., approximately four peak-widths away from the ^{208}Pb mass position) and values reported are background corrected. All measurements were performed on a single EPT® discrete-dynode electron multiplier operated in pulse counting

This is a preprint, the final version is subject to change, of the American Mineralogist (MSA)
Cite as Authors (Year) Title. American Mineralogist, in press.
DOI: https://doi.org/10.2138/am-2019-6516

mode. Pb concentrations were calculated using ^{208}Pb, with count rates normalized to S_2. The average background for the electron multiplier on all unknowns and reference materials for session D1 was 0.6±0.6 counts per second (cps), 0.3±0.2 cps for session D2, and 0.15±0.09 cps for session D3. We also measured $^{80}Se^{+}$, $^{232}Th^{16}O^{+}$ and $^{238}U^{16}O^{+}$, but these are not reported because concentration data do not exist for the standards and/or count rates were close to background levels.

Pb calibrations, error estimation, and data reduction

Three synthetic doped reference materials (Supplemental Table S1) were used to determine Pb concentrations. JB-MSS1 and JB-MSS5 are synthetic FeS with Pb concentrations measured by solution ICP-MS (Dare et al., 2010; Patten et al., 2013), while UQAC-MSS1 is a synthetic $NiFeS_2$ with Pb concentration measured by LA-ICPMS (Dare et al., 2011). Trace element concentrations were calculated using a linear calibration curve (Fig. 1A), defined by plotting X_i/S_2 measured on the SHRIMP-RG versus the accepted concentration of element X_i in ppm for the three reference materials. We used the data-defined intercept (i.e., not fixed at zero; Fig. 1A) of the Pb calibration curve to estimate the lower limit of detection for each session: 2.2 ppm for session D1, 2.0 ppm for session D2 and 2.3 ppm for session D3.

The sulfide UQAC-MSS1 is the lowest concentration Pb reference material available (2.0±0.4 ppm) and is the most representative of the range of concentrations in the unknown samples analyzed in this study. However, the relatively large scatter in measured $^{208}Pb/^{64}S_2$ for UQAC-MSS1 indicates poor reproducibility near the detection limit: the 1σ standard deviation for UQAC-MSS1 was 129% for session D1 (n=7), 79% for session D2 (n=12), and 89% for session D3 (n=16). Compared to unknown samples, the measured background was higher on

UQAC-MSS1 due to tailing from the Fe_2S_3 peak 0.191 AMU below the ^{208}Pb peak: 1.9±0.5 cps for session D1, 0.7±0.1 cps for session D2, and 0.3±0.1 cps for session D3. This may explain the increased scatter and uncertainty of UQAC-MSS1, which is currently the limiting factor for improving the detection limit for Pb concentration analyses.

Measurement error is typically calculated based on Poisson counting statistics, however this error estimate is small in comparison to the reproducibility of the reference materials. Therefore, instead of using the count statistics (i.e. internal error), we use external error based on the reproducibility of the measured ratios of the reference materials. Because we only have three reference materials (JB-MSS1, JB-MSS5, and UQAC-MSS1), external error was calculated by the exponential fit of the one-sigma standard deviation (%) of the measurements of the reference material versus accepted concentration (Fig. 1B). This method of calculating error is reasonable given the limited number of available reference materials and the higher uncertainty associated with lower concentration samples.

Sulfides were re-imaged after analysis using backscattered and secondary electron imaging on the SEM to check spot placement. Every point was visually checked and Pb concentration data excluded when the spot was not entirely on a sulfide or if the spot was directly on crack(s) within the sulfide. Low S_2 counts usually occurred in conjunction with spots located near grain edges or on cracks, which may reflect desulfurization during alteration that leads to the formation of native iron and iron hydroxides (Luguet et al., 2003).

Sulfide trace elements measured by SHRIMP-RG with the Cs^+ source

Most non-metals, metalloids and transition metals have low secondary ionization efficiency using an O_2^- beam (Wilson, 1995), and were instead measured with the SHRIMP-RG

This is a preprint, the final version is subject to change, of the American Mineralogist (MSA)
Cite as Authors (Year) Title. American Mineralogist, in press.
DOI: https://doi.org/10.2138/am-2019-6516

in two analytical sessions using a Cs^+ primary beam. Only a subset of grains was analyzed during these sessions due to time limitations, with most of the first session (session C1) spent on development of the analytical technique. The beam current during the session C1 ranged from 5 to 10 nA, while during session C2 it ranged from 3 to 6 nA. Negatively charged secondary ions were sputtered from a spot that was ~20 μm diameter and ~4 μm deep. Prior to each measurement, we rastered the primary beam over an area 45x45 μm for 90–120 s to minimize surface contamination.

All measurements were performed with a mass resolution of 9000–9500 (10% peak height criteria). This mass resolution was sufficient to resolve the major overlapping interferences for the masses of interest. In session C1, measured masses included $^{35}Cl^-$, $^{67}S_2^-$, $^{80}As^-$, $^{80}Se^-$, $^{96}S_3^-$, $^{121}Sb^-$, and $^{130}Te^-$, with Cl included among the siderophile/chalcophile elements as a potential indicator of alteration. The mass table also included $^{101}Ru^-$, $^{103}Rh^-$, $^{106}Pd^-$, $^{107}Ag^-$, $^{108}Pd^-$, $^{189}Os^-$, $^{193}Ir^-$, and $^{195}Pt^-$, but these were not included in the second session because ^{189}Os, ^{193}Ir and ^{195}Pt yielded very low counts, while ^{101}Ru, ^{103}Rh, ^{106}Pd, ^{107}Ag, and ^{108}Pd had overlapping isobaric interferences that could not be fully resolved. In the second session, we added $^{30}Si^-$ to monitor beam overlap with silicate minerals, $^{197}Au^-$, and $^{107}Ag^{32}S^-$ instead of $^{107}Ag^-$, which can be better resolved from isobaric interferences but has lower sensitivity. Masses for each element were measured with one peak-hopping cycle through the run table, with counting times of 4–20 s.

Trace element calibrations, error estimation, and data reduction

Count rates for each element were normalized to either S_3 (session C1) or S_2 (session C2). Both normalizing methods minimize the effects of variations in beam intensity, though S_2

This is a preprint, the final version is subject to change, of the American Mineralogist (MSA)
Cite as Authors (Year) Title. American Mineralogist, in press.
DOI: https://doi.org/10.2138/am-2019-6516

yields more reproducible ratios. Following the approach from Pb measurements, we excluded analyses if the total counts of S_2 or S_3 deviated by more than two-sigma from the average for a given session. In addition, some analyses of As and Te were excluded as they had counting statistic errors >70%, suggesting they were at or below the limits of detection.

Trace element calibration curves were calculated using five reference materials: UQAC-MSS1, JB-MSS1, JB-MSS5, FeS-1 and FeS-8 (Supplemental Table S1). The first three reference materials are the same ones used for Pb analysis with the O_2^- source. The measured reference values (Supplemental Table S1) for these materials are based on a combination of solution and LA-ICPMS measurements (Barnes, pers. comm., 2017; Dare et al., 2010, 2011; Duran et al., 2016; Patten et al., 2013). FeS-1 and FeS-8 are doped synthetic troilites that were measured by LA-ICPMS by Hayden et al. (2011). As no published values were available for Cl in any of the reference materials, we use a value of 50 ± 20 ppm determined by electron microprobe analysis on FeS-8 using the JEOL JXA-8230 probe at Stanford University.

Count rates of the reference materials, normalized to either S_2 or S_3, were used to define linear working curves for each element (Supplemental Figure S2). Similar to Pb measurements, reported errors for trace element concentrations are based on the exponential fit to the one-sigma standard deviation (%) of the measured ratio for reference material versus accepted concentration (Supplemental Fig. S2). This is true for all elements, except for Se and Ag, where error increases linearly with increasing concentration, perhaps due to heterogeneity in the higher concentration reference materials. Further details of the calibration, error propagation, and data reduction for each element are provided in the supplemental methods.

RESULTS

This is a preprint, the final version is subject to change, of the American Mineralogist (MSA)
Cite as Authors (Year) Title. American Mineralogist, in press.
DOI: https://doi.org/10.2138/am-2019-6516

A total of 152 base metal sulfides from 11 peridotites and 1 pyroxenite were measured for Pb abundances, of which 76 sulfides were also measured for other trace elements (As, Se, Sb, Te, Ag, Au, and Cl). As these seven elements were measured in spots adjacent to the Pb analytical spots, Pb data cannot be directly compared to other elements in an individual analysis, particularly as several elements show considerable intra-grain heterogeneity. To allow comparison of the trace and major element datasets, data are presented on a grain-averaged basis in Tables 2–4, while individual analyses are presented in Supplemental Tables S3 and S4. Some grains show large standard deviations in Tables 3 and 4, which reflects intra-grain variability, while analytical precision is represented by the errors reported in Supplemental Tables S3 and S4 for the individual analyses.

Sulfide petrology and mineralogy

The morphology, composition, and mineralogy of the analyzed sulfides were constrained using a combination of petrographic photomicrographs, backscattered electron images, and EDS maps (Fig. 2), combined with EMPA and SHRIMP-RG major element analyses (Tables 2–4). Sulfides occur either as intergranular grains (Fig. 2A–B) or as inclusions within silicates (Fig. 2D–E). The majority of grains are intergranular (77%), distributed through multiple phases or along grain boundaries. Among the sulfides that are inclusions (23% of all sulfides), half (12% of all sulfides) are enclosed either within olivine or orthopyroxene, while the rest are enclosed within clinopyroxene, often in association with spinel (Fig. 2D). This latter textural relationship has previously been interpreted to represent late-stage crystallization of silicate and sulfide melts in the lithosphere (e.g., Luguet et al., 2003).

Sulfides in our samples occur either as individual sulfide grains (Fig. 2A) or as clusters of sulfide grains (Fig. 2C). Clusters are defined on the basis of multiple sulfides occurring within ~200 μm of each other. In the tables and figures, sulfide numbers with a letter suffix indicate one sulfide grain within a cluster, each of which was large enough (>20 μm) for *in situ* analysis (Fig. 2C). Some sulfide clusters are distributed throughout a host grain, for example along exsolution lamellae in pyroxene or as small blebs, all of which were too small for analysis. Out of 150 sulfide grains analyzed, the majority was classified as clusters (65%) and the remainder as individual grains. However, the occurrence of clusters versus individual grains varies on a sample-by-sample basis. In almost two-thirds of the samples, >60% of analyzed sulfides occur as clusters, while in one-third of samples, >60% of sulfides are individual grains.

Major element analyses of sulfides from each category are reported in Table 2. This data, combined with the EDS maps, was used to categorize sulfides into three groups: 1) pentlandite (Pn = $(Fe,Ni)_9S_8$) sulfides (Fig. 2); 2) isolated chalcopyrite and distributed Cu-bearing sulfides (Fig. 3); or 3) altered sulfides (Fig. 4). The majority of sulfides (82 out of 150) are in the first category, with Fe contents of 31–47 wt%, Ni of 18–34 wt% and rarely >1 wt% Cu (Table 2). However, EDS images reveal that in some grains, very small (~1 μm) Cu enriched veins or patches are present, often near the rim or along cracks (Fig. 3E-F).

The second category of sulfides consists of pentlandite with Cu intergrowths that occur either as isolated discrete phases within the pentlandite grain (Fig. 3A–B) or distributed throughout the pentlandite grain (Fig. 3C–F). Major element analysis of the discrete Cu phases (Table 2) indicates that they are chalcopyrite ($CuFeS_2$), hosted in pentlandite. In other grains, Cu enrichments are either pervasively distributed within the grain (Fig. 3C–D) or occur as smaller needle-like lamellae (Fig. 3E–F). For both occurrences of Cu-bearing phases in pentlandite, the

Cu concentrations range from 0.2 to 19 wt% Cu. The very low abundance of Cu in some analyses suggests the occurrence of a Cu-bearing phase (possibly chalcopyrite) intergrown with pentlandite at a length-scale not resolvable by EMPA analysis (e.g., <1 μm).

The third category is composed of altered sulfides, identified based on the presence of iron hydroxides (Fig. 4A), mottled textures (Fig. 4B–C), or pervasive cracks (Fig. 4D). Most sulfides in this category were classified as altered based on petrographic analysis (Fig. 4) and relatively high oxygen contents (1.4–26 wt% O determined by EMPA; Table 2). In addition, 14 sulfides were identified as altered based on oxygen contents >1 wt% and ranging up to 13 wt%, but no clear textural evidence for alteration. An oxygen content of >1 wt% was used as the threshold to distinguish between altered and unaltered grains, as the equilibrium content for oxygen in sulfides is <1 wt% O (Kiseeva and Wood, 2013) for the estimated 7 wt% FeO of SWIR primary magmas (Birner et al., 2018). Alteration phases and cracks were avoided during SHRIMP-RG analysis wherever possible. However, alteration in some samples was so extensive that the remaining pentlandite grains were too small to analyze (e.g., HLY0102-70-62) or cracks too extensive to avoid.

Pb concentrations in sulfides

In total, we measured Pb concentrations in 152 sulfides (Fig. 5), of which seven were from Gakkel Ridge and four from SWIR. Grain-averaged Pb concentration data are reported in Table 3 for unaltered grains and Table 4 for altered grains. All individual analyses are reported in Supplemental Table S3. While individual analyses have relatively large error due to the lack of low concentration sulfide reference materials, Pb concentrations within a grain are generally reproducible from one spot to another.

This is a preprint, the final version is subject to change, of the American Mineralogist (MSA)
Cite as Authors (Year) Title. American Mineralogist, in press.
DOI: https://doi.org/10.2138/am-2019-6516

Lead concentrations range from 2.0 to 36.2 ppm for the 108 unaltered sulfides in this study (Fig. 5A). These values overlap the range previously determined by Warren and Shirey (2012) for 15 sulfides from the same two ridges (Fig. 9). However, Warren and Shirey (2012) reported concentrations as low as 0.1 ppm Pb, measured by isotope dilution thermal ionization mass spectrometry (ID-TIMS), which has a lower detection limit for Pb in sulfide than ion microprobe. Using the SHIRMP-RG, the majority of grains that we analyzed yielded count rates for Pb that were higher than the noise on the detector (~0.3 cps), indicating that Pb is present in our sulfides above the SHRIMP-RG limit of detection. Our average pentlandite concentration of 2.9 ppm Pb is resolvable above the low concentration reference material UQAC-MSS1, which has 2 ppm Pb (Dare et al., 2011) and higher backgrounds (≤1.9 cps) due to tailing from the Fe_2S_3 peak. Improved precision for sulfide Pb concentrations requires more sulfide reference materials to become available at low Pb abundances.

The majority of sulfides in this study are pentlandites and their Pb concentrations are plotted in Fig. 5A. These sulfides have concentrations ranging from 2.0 to 5.9 ppm Pb, with an average concentration of 2.9±0.8 ppm (n=82 grains), indicating consistently low Pb. Comparison of the two ridges indicates no significant difference within our sample set: Gakkel sulfides have an average of 3.0±0.8 ppm Pb (n=71), while SWIR sulfides have an average of 2.7±0.3 ppm Pb (n=11 grains).

In addition to pentlandite, some sulfides in this study contain a mixture of chalcopyrite and pentlandite, which was found in eight samples. Cu-bearing sulfides are divided into two categories based on whether they occur as discrete chalcopyrite grains within pentlandite grains (Fig. 3A–B) or as a distributed Cu-bearing phase (Fig. 3C–F), which may be submicron intergrowths of a Cu-Fe sulfide (chalcopyrite or bornite) with a Fe-Ni sulfide (pentlandite or

pyrrhotite). The overall concentration range of the Cu-bearing grains is 2.2–36.2 ppm (Fig. 6), with an average of 7.9 ppm Pb (n=27 grains), which is 5 ppm higher than the pentlandite population.

Isolated chalcopyrite inclusions within pentlandite grains were found in only two samples (PS59-235-18 and Van7-96-21V) at sizes large enough to analyze, though usually only one analysis could be performed (Table 3). These chalcopyrite grains have an average of 3.6±1.3 ppm Pb (n=4 grains), compared to the pentlandite hosts for these chalcopyrites, which have 3.1±1.0 ppm Pb (n=4 grains).

Pb concentrations are homogeneous, within analytical precision, in all pentlandites, while five of the 27 Cu-bearing sulfides have measurable heterogeneity (Fig. 6). This variability is found in sulfides that have sub-micron scale intergrowths of pentlandite and a Cu-bearing phase. Hence, this variation may reflect preferential partitioning of Pb into the Cu enriched phase relative to pentlandite, as suggested by data from sulfide ore deposits (Dare et al., 2010, 2011; Duran et al., 2016). However, testing this requires mapping with a technique that has both high spatial resolution and high sensitivity.

Altered domains within sulfides and a few completely altered grains were analyzed by SHRIMP-RG. Overall, altered sulfides (Table 4) have a range of 2.5–48.6 ppm Pb (Fig. 5B), with an average of 9.7 ppm Pb (n=43). The higher average Pb concentration of altered sulfides compared to unaltered sulfides suggests that alteration increases Pb abundances. Nine of the 44 altered sulfides were identified as containing variable Pb abundances (Table 4). Grains with abundant cracks have a higher average Pb concentration of 15±14 ppm Pb (n=14; Table 4), similar to the observation by Duran et al. (2016) that Pb is higher in the region of cracks in pentlandite from ore deposits.

One peridotite sample (PS59-235-01) from the Gakkel Ridge was investigated in detail to look for sub-sample variations in Pb concentrations. This sample contains all three categories of sulfides, including hydrothermally altered sulfides, despite having a low degree of serpentinization. Pentlandites from this sample span the largest Pb concentration range (2.0 to 5.7 ppm, n=25) compared to other samples (Fig. 5A), though the grains themselves are homogeneous, except where altered. The majority (92%) of these grains contain 2.0 to 3.5 ppm Pb, with only two sulfides containing >3.5 ppm Pb. The Cu-bearing sulfides in this sample have higher Pb concentrations than the pentlandites, with a range of 8.3–15.4 ppm Pb (n=3) (Fig. 6). The altered sulfides have a wide range of concentrations, from 4.6–44.4 ppm (n=6 grains), with an overall higher average concentration (16.0 ppm), similar to the global average for altered grains.

SWIR dredge Van7-96 was analyzed in detail to explore dredge-scale variations in sulfide Pb contents. The 23 analyzed sulfides have a large concentration range (0.9–36.2 ppm Pb) and higher average Pb (8.4 ppm) compared to the entire sulfide population. Sample Van7-96-28 contains the highest concentration sulfide measured both in this study (36 ppm Pb) and by Warren and Shirey (2012) (12 ppm Pb). Dredge Van7-96 also contains 56% of the Cu-bearing sulfides identified in this study. As this dredge contains pyroxenite veins and both the peridotites and pyroxenites have enriched trace element abundances (Warren et al., 2009), the higher Pb content and the abundance of chalcopyrite in this dredge probably reflects melt-rock interaction.

The Pb range for all unaltered sulfides (both Pn and Cu-bearing) is 2.0–36.2 ppm, with an average of 4.1 ppm Pb (n=111 grains). The range of all sulfides in this study (unaltered and altered) is 2.0–48.6 ppm, with an average of 5.6 ppm Pb (n=156 grains), which corresponds to the potential contribution of sulfides in a bulk rock analysis of an altered abyssal peridotite.

447

448 **Other trace element concentrations in sulfides**

449 Trace element concentrations of Se, Te, As, Sb, Ag, Au, and Cl are reported on a grain-
450 averaged basis in Table 3 (unaltered sulfides) and Table 4 (altered sulfides), while individual
451 analyses are reported in Supplemental Table S4.

452 The concentration ranges of trace elements in Pn and Cu-bearing sulfides are shown Fig.
453 7. We plot grain averages so that these elements can be directly compared to Pb (Table 3), which
454 required different analytical spots, and to limit the bias from larger grains with more analyses.
455 However, most elements have large intra-grain heterogeneities, with up to two orders of
456 magnitude variation in As, Sb, and Cl, while Ag and Te have up to one order of magnitude
457 variation in concentration. In contrast, Se and Au have homogeneous concentrations, with the
458 exception of a Cu-bearing sulfide (Van7-96-28, Sulfide 14), which includes the highest Au
459 concentration (770 ppb) of the dataset.

460 Trace element concentration ranges in unaltered sulfides are 45–250 ppm Se, <4–360
461 ppm Te, <1.5–1900 ppm As, 2–420 ppm Sb, 2–340 ppm Ag, 2–770 ppb Au, and 0.2–1000 ppm
462 Cl (Fig. 7). Compared to other trace elements, Au is two to three orders of magnitude lower in
463 concentration. In Cu-bearing sulfides, the elements Ag, As, and Sb sometimes have higher
464 concentrations than in pentlandite sulfides, while Se and Te have similar concentration ranges
465 (Fig. 7), but more data is needed to confirm this observation. No significant compositional
466 difference between the two ridges is observed.

467 Trace element concentration ranges in altered sulfides are 47–500 ppm Se, <4–160 ppm
468 Te, <1.5–3800 ppm As, 20–930 ppm Sb, 9–490 ppm Ag, 11–200 ppb Au, and 1–12000 ppm Cl
469 (Fig. 7). All elements, except Te and Au, extend to higher concentrations among altered grains

compared to unaltered. The average concentrations of Se, Te, and Au are not significantly different between unaltered and altered grains, with Te having the same average while the other two elements are increased by a factor of <1.6. In contrast, the averages for As, Sb, Ag, and Cl are higher by a factor of 2 or more, with the average Cl concentration increased by a factor of 7.

DISCUSSION

Effect of hydrothermal alteration on sulfides

As most abyssal peridotites have undergone hydrothermal alteration and seafloor weathering (e.g., Bach and Früh-Green, 2010; Klein et al., 2015), we first assess the effects of hydrothermal alteration on sulfides before exploring their higher temperature history. Most samples in this study are hydrothermally altered, with the most altered sample (HLY0102-70-75) having undergone ~75% serpentinization (D'Errico et al., 2016). However, we also analyzed four Gakkel samples from dredges PS59-235 and -238 that have minimal levels of serpentinization. Despite this, hydrothermally altered sulfides are present in these samples, suggesting that sulfides are more susceptible to hydrothermal alteration than silicate minerals.

Secondary sulfides, iron oxides (such as magnetite), iron hydroxides and alloys (such as awaruite) can form during hydrothermal circulation, either by direct precipitation from fluids or by sulfur-loss from high temperature sulfides (Klein and Bach, 2009). Altered grains in this study are mainly pentlandites that have been partially replaced by iron hydroxides, which in extreme cases result in relict pentlandite interiors surrounded by alteration rims of iron hydroxide (Fig. 4A), similar to observations by Luguet et al. (2003) for sulfides in MAR abyssal peridotites. In other grains, EMPA analyses revealed high oxygen contents (up to 19 wt%), suggesting oxidation during weathering. In sample PS59-201-39, sulfide 3 (Fig. 4B) may be

493 hydrothermal in origin due to its euhedral shape and vermicular internal texture, which is similar
494 to observations of a MAR hydrothermal sulfide described by Luguet et al. (2003). Overall, we
495 did not identify secondary alteration minerals such as awaruite, heazlewoodite, or pyrite, which
496 have been found in abyssal peridotites that have undergone very high levels of hydrothermal
497 alteration (e.g., Alt and Shanks, 2003; Bach et al., 2003; Klein and Bach, 2009). However,
498 sulfides with mottled or vermicular textures and in alteration veins were purposefully avoided
499 when selecting grains for analysis.

500 Sulfides with alteration have higher and more variable Pb concentrations (range of 2.5–
501 48.6 ppm, average of 10 ppm, n=43) than unaltered sulfides (range of 2.0–36.2 ppm, average of
502 4 ppm, n=111), as shown in Fig. 5. This increase in Pb abundance is likely due to hydrothermal
503 alteration adding external Pb to the sulfides. Hydrothermal vent fluids have elevated Pb
504 concentrations relative to seawater (Tatsumoto and Patterson, 1963; Metz and Trefry, 2000;
505 Tivey, 2007) and hydrothermal sulfides that precipitate out of vent fluids can have Pb
506 concentrations >0.65 wt% (Kadko et al., 1985; Tivey et al., 1995).

507 The elements As, Sb, Ag, and Cl also have increased concentrations in altered grains and
508 show significant intra-grain heterogeneity. This suggests that the observed heterogeneity is due
509 to hydrothermal alteration, whereas Pb, Se, and Au – all of which are generally homogeneous –
510 are not as easily modified. This conclusion agrees with LA-ICPMS maps of Pb and Ag
511 distributions in pentlandite ore grains by Duran et al. (2016), which show greater heterogeneity
512 in Ag relative to Pb, with both elements having increased abundances near cracks and grain
513 boundaries. Trace element mapping of our sulfides would provide more constraints on intra-
514 grain variations, including whether concentrations increase near cracks.

This is a preprint, the final version is subject to change, of the American Mineralogist (MSA)
Cite as Authors (Year) Title. American Mineralogist, in press.
DOI: https://doi.org/10.2138/am-2019-6516

Tellurium is the outlier among elements with intra-grain heterogeneity, as it does not have higher concentrations among the altered dataset (average of 27 ppm Te) relative to the unaltered dataset (also average of 27 ppm Te). Instead, the intra-grain range in Te concentrations suggests the presence of telluride micro- or nano-phases, as Te is highly incompatible in MSS and often forms telluride phases (Helmy et al., 2007, 2010; Lorand et al., 2010). Antimony may also be present in these phases, but the lack of a correlation between individual Te and Sb analyses (Table S4) suggests that Sb was modified by hydrothermal alteration. The influence of discrete Te phases on sulfide Se/Te systematics is discussed below.

For the purposes of exploring high temperature mantle processes, we exclude altered sulfides from further discussion.

Sulfide petrogenesis

Base metal sulfides analyzed in this study consist predominantly of pentlandite with minor chalcopyrite. Previous studies of abyssal peridotites have found that pentlandite is the dominant phase, with minor chalcopyrite and pyrrhotite, plus a range of secondary sulfide minerals produced by hydrothermal alteration (Luguet et al., 2001, 2003; Alard et al., 2005; Klein and Bach, 2009; Liu et al., 2009). Peridotite-hosted sulfides are derived from MSS, the main form of sulfide in the mantle, which is not stable at low pressure and temperature. Experimental constraints on MSS within the range of natural mantle compositions indicate that MSS is entirely molten in the upper 250 km of the mantle (Tsuno and Dasgupta, 2015; Zhang and Hirschmann, 2016), as shown in Fig. 8A. During melt segregation, sulfide melt is entrained as immiscible droplets in silicate melt (Holzheid et al., 2000; Bockrath et al., 2004).

This is a preprint, the final version is subject to change, of the American Mineralogist (MSA)
Cite as Authors (Year) Title. American Mineralogist, in press.
DOI: https://doi.org/10.2138/am-2019-6516

537 During cooling, sulfide melt undergoes a combination of 1) crystallization of sulfide
538 minerals (Fig. 8) and 2) dissolution into silicate melt due to the increasing solubility of sulfur in
539 silicate melt with decreasing pressure (Mavrogenes and O'Neill, 1999). Sulfide minerals have
540 been found in both abyssal peridotites and MORBs, but they have a different petrogenesis due to
541 their different paths to the surface. In MORB, sulfide crystallizes at low pressure, but high
542 temperature, when magma erupts and is quenched on the seafloor. The formation of sulfide in
543 this system depends on whether the silicate magma is sulfur-saturated upon eruption (referred to
544 as "sulfur content at sulfide saturation"). Previous studies of sulfide globules in MORB glasses
545 have identified mineral assemblages consisting of MSS (Fe-Ni sulfide) and intermediate solid
546 solution (ISS; Cu-Fe sulfide) with minor pentlandite (e.g., Czamanske and Moore, 1977; Patten
547 et al., 2012; Yang et al., 2014), suggesting crystallization of sulfide at ~1000–1100°C from a
548 sulfur-saturated silicate melt.

549 Uplift of peridotite to the ocean floor is slow and sulfide crystallization in peridotite
550 occurs at relatively high pressure, where the amount of sulfur required for sulfide saturation is
551 low (Mavrogenes and O'Neill, 1999), and with time available for the sulfide melt to undergo
552 fractional crystallization followed by subsolidus re-equilibration. We estimate that sulfide
553 crystallization occurred at ~1 GPa and ~1050–1200°C, based on the sulfide melting experiments
554 of Zhang and Hirschmann (2016) and our geotherm for an ultra-slow spreading ridge (Fig. 8).
555 Observations from experiments (e.g., Kullerud et al., 1969; Fleet, 2006; Peregoedova and
556 Ohnenstetter, 2002) and natural samples (e.g., Szabó and Bodnar, 1995; Luguet and Reisberg
557 2016) indicate that Fe-rich MSS crystallizes initially, resulting in a Ni-Cu-rich sulfide melt. At
558 lower temperature, this melt and MSS react to produce other solid solution sulfides. These
559 subsequently undergo subsolidus re-equilibration to assemblages dominated by pentlandite,

pyrrhotite, and chalcopyrite, with the phase assemblage depending on the extent to which the sulfide melt fractionated prior to crystallization.

Previous studies of abyssal, orogenic, and xenolith peridotites have developed a framework to classify the range of sulfide occurrences in peridotites (Szabó and Bodnar, 1995; Alard et al., 2000, 2002, 2011; Lorand et al., 2003, 2004; Lorand and Luguet, 2013, Luguet and Reisberg, 2016). Type 1 sulfides consist of MSS, pyrrhotite, pentlandite, and minor Cu-bearing sulfides and are typically found as rounded inclusions in olivine or orthopyroxene in xenoliths (e.g., Alard et al., 2000; Luguet and Reisberg, 2016). Due to their composition and occurrence as inclusions in silicate phases that do not melt to completion, Type 1 sulfides are often referred to as residual and are interpreted to have undergone the least modification during mantle melting. Type 2-4 sulfides are typically intergranular or occur as inclusions in metasomatic silicates and are interpreted to have formed by crystallization from percolating melts of various compositions (e.g., Luguet and Reisberg, 2016). In particular, Type 2 sulfides are defined as consisting of mostly pentlandite and chalcopyrite, with minor MSS and pyrrhotite, and occurring either as intergranular or included phases (e.g., Luguet and Reisberg, 2016).

In this study, we classify all of our sulfides as Type 2 on the basis of their compositions and textural occurrences. Compositionally, the sulfides are Ni-poor and Fe-rich ($1.0<Fe/Ni<2.7$) pentlandite with minor chalcopyrite. MSS and pyrrhotite have not been identified, though pyrrhotite has been identified in other Gakkel samples by Liu et al. (2009), while any MSS would have undergone subsolidus re-equilibration to pentlandite and pyrrhotite. Our observation is similar to the assemblage of Pn + Cu-bearing sulfides in SWIR and MAR peridotites identified by Luguet et al. (2001), which they concluded formed by subsolidus re-equilibration after crystallization from a sulfide melt.

583 Morphologically, most sulfides in our samples are intergranular and occur as clusters of
584 grains. In addition, half of our included sulfides occur in clinopyroxene, which itself may have
585 crystallized from a silicate melt. Hence, we interpret the sulfides in our samples to have formed
586 by fractional crystallization from a sulfide melt that became increasingly enriched in Cu. Given
587 the evidence for silicate melt addition in our peridotites (Warren et al., 2009; D'Errico et al.,
588 2016), we conclude that the peridotites interacted with relatively low volumes of sulfide melts
589 and silicate melts that crystallized at depth (~30 km; Fig. 8C). This interpretation of melt
590 infiltration and crystallization agrees with previous investigations of Cu-bearing sulfides in
591 peridotites (Guo et al., 1999; Alard et al., 2000; Luguet et al., 2001; Lorand and Alard, 2001;
592 Lorand et al., 2003).
593
594 **Pb in mantle sulfides**
595 Among the unaltered mantle sulfides in this study, the majority are pentlandite (n=86)
596 with an average Pb concentration of 2.9±0.8 ppm (Fig. 5A). As discussed above, this value is
597 close to, but resolvable above, the detection limit. The remainder of the population consists of
598 Cu-bearing sulfides (n=27) with a Pb range of 2.2–36.2 ppm and average of 8 ppm (Fig. 6). Cu-
599 bearing sulfides are derived from more evolved sulfide melts than pentlandite, as Cu is
600 incompatible in MSS relative to sulfide melt and concentrates in sulfide melt during fractional
601 crystallization (e.g., Barnes et al., 1997; Naldrett et al., 1982; Peregoedova and Ohnenstetter,
602 2002). Hence, higher Pb concentrations are expected in Cu-bearing sulfides than in pentlandite
603 (Fig. 6) as $D_{Pb}^{\text{MSS/sulfide melt}}$ is 0.005 (Li and Audétat, 2015; Brenan, 2015). However, not all Cu-
604 bearing sulfides have high Pb contents and Cu concentrations in sulfide are not correlated with
605 Pb concentrations.Results from this study are similar to previous measurements of Pb

concentrations in other abyssal peridotite sulfides (Fig. 9). Warren and Shirey (2012) measured a range of 0.1 to 12 ppm among 15 grains from SWIR and Gakkel peridotites. Burton et al. (2012) measured a range of 2 to 8 ppm among 8 grains from the Fifteen Twenty Fracture Zone on the Mid-Atlantic Ridge. Combining data from this study with these studies, Gakkel sulfides have an average of 3.2 ppm Pb, SWIR sulfides have 5.9 ppm, and MAR sulfides have 4.7 ppm (Fig. 9). However, this comparison is based on only 16 samples from 10 locations (5 Gakkel dredges, 4 SWIR dredges, and 1 MAR drill core), which is not enough to determine if systematic differences exist among these ridges.

The concentrations of Pb in MORB glasses and in sulfides globules crystallized in MORB are shown in Fig. 9 relative to the peridotite sulfide dataset. Basalt glasses have low concentrations compared to sulfides, with a normal MORB average of 0.51±0.03 ppm Pb (n=291), based on the compilation by Gale et al. (2013). The presence of sulfide globules in many MORBs indicates that these silicate melts erupt at or close to sulfide-saturation (Mathez, 1976; Czamanske and Moore, 1977; Francis, 1990; Patten et al., 2012; Yang et al., 2014). Very few sulfide globules have been analyzed for trace elements, though Patten *et al.* (2013) determined a range of 12–22 ppm Pb for seven globules measured by LA-ICPMS. This range confirms that Pb is compatible in sulfide melt relative to silicate melt and agrees with experimentally determined values for $D_{Pb}^{\text{sulfide melt/silicate melt}}$ of 14–48 (Li and Audétat, 2012), 2–165 (Kiseeva and Wood, 2013, 2015), 10–57 (Brenan, 2015), and 4–67 (Hart and Gaetani, 2016). In the next section, we evaluate the complex relationship that exists between Pb in abyssal peridotite sulfides and in basaltic melts due to the presence of two immiscible melts and the changing saturation of sulfide in silicate melt as these melts rise through the mantle.

This is a preprint, the final version is subject to change, of the American Mineralogist (MSA)
Cite as Authors (Year) Title. American Mineralogist, in press.
DOI: https://doi.org/10.2138/am-2019-6516

Evolution of Pb during sulfide petrogenesis at ridges

Sulfides in abyssal peridotites from mid-ocean ridges are the result of sulfide melting followed by fractional crystallization of sulfide melts, as illustrated in Fig. 8. When the silicate portion of the mantle undergoes adiabatic decompression melting beneath a mid-ocean ridge, the evolution of the sulfide melt depends on the solubility of sulfur in silicate melt (e.g., Mavrogenes and O'Neill, 1999; Smythe et al., 2017). As silicate melt volume increases, sulfide melt volume decreases, as some sulfur partitions into the silicate melt as a function of sulfur solubility in silicate melt. In addition, due to the negative pressure dependence of sulfur solubility in silicate melt (Mavrogenes and O'Neill, 1999), more sulfur will partition into silicate melt as these melts rise through the mantle. Hence, as sulfide melt begins to cool at shallower depth, it will undergo both fractional crystallization to form sulfide and sulfur dissolution into silicate melt. Due to this behavior, the evolution of Pb in these melts depends on the partitioning of Pb between sulfide and sulfide melt (e.g., $D_{Pb}^{\text{MSS/sulfide melt}} = 0.005$; Brenan, 2015), and between sulfide melt and silicate melt (e.g., $D_{Pb}^{\text{sulfide melt/basalt}} = 17$; Brenan, 2015). In contrast, MORB sulfide globules are consistent with batch crystallization of a sulfide melt upon quenching of a sulfur-saturated silicate melt, governed by $D_{Pb}^{\text{sulfide melt/basalt}}$.

This study constrains the Pb concentration in sulfides that crystallize out of a sulfide melt and back into the mantle beneath mid-ocean ridges. Combining the results of this study with previous studies (Burton et al., 2012; Warren and Shirey, 2012), abyssal peridotite sulfides have a range of 0.1 to 36 ppm Pb, with an average of 4 ppm (n=136 grains). As these sulfides have undergone subsolidus re-equilibration to pentlandite and Cu-bearing phases, some of this concentration range may reflect redistribution during re-equilibration. Hence, we interpret the

651 average concentration of 4 ppm Pb to be representative of the amount of Pb left in sulfides in the
652 mantle after processing through the mid-ocean ridge system.

653 Previous studies (e.g., Meijer et al., 1990; Hart and Gaetani, 2006) have suggested that
654 mantle Pb is predominantly hosted in sulfides prior to the onset of melting. We evaluate this
655 possibility by constructing a model where we assume that the initial sulfide melt contains all
656 mantle Pb. We then calculate the amount of fractional crystallization necessary to produce 4 ppm
657 Pb in sulfide during fractional crystallization of a sulfide melt at shallow depth (e.g., 1 GPa; Fig.
658 8) beneath the ridge. We do not model the evolution of sulfur itself in the sulfide melt-silicate
659 melt system, which is a complex process (e.g., Mavrogenes and O'Neill, 1999; Holzheid and
660 Grove, 2002; Ariskin et al., 2013; Smythe et al., 2017).

661 The initial Pb content of our sulfide melt is based on estimates for the amount of Pb in the
662 mantle prior to any melting. We used two types of estimates: 1) the estimate of 75 ppm Pb
663 hosted in mantle sulfide from Hart and Gaetani (2006) and 2) estimates of Pb in the depleted
664 mantle (DM) of 0.023 ppm (Salters and Stracke, 2004) and 0.018 ppm (Workman and Hart,
665 2005). Assuming that all Pb in DM was initially hosted in sulfide, DM Pb estimates were
666 converted to initial amounts of Pb in sulfide melt using the estimated DM sulfide modal
667 abundance of 0.05% (Hart and Gaetani, 2006). This translates to concentrations of 46 and 36
668 ppm Pb, respectively.

669 We model the evolution of Pb in the sulfide-sulfide melt system using modal fractional
670 crystallization equations (e.g., Gast, 1968; Shaw, 1970) to calculate the concentration of Pb in a
671 crystallizing sulfide (C_S) and the remaining sulfide melt (C_L). Modal melting is used here as a
672 simplification for the complex sequence of sulfide phases that crystallize from a sulfide melt,

673 which involve reactions both suprasolidus and subsolidus (e.g., Kullerud et al., 1969;
674 Peregoedova and Ohnenstetter, 2002).

675 Our model requires a value for the Pb partition coefficient between sulfide and sulfide
676 melt ($D_{Pb}^{\text{MSS/sulfide melt}}$), which depends on the composition, oxygen fugacity, sulfur fugacity,
677 pressure, and temperature of the system. Two experiments from Brenan (2015) provide the
678 closest overlap to the estimated conditions for crystallization of our sulfides, having been run at
679 1200–1250°C, 1.5 GPa, and conditions slightly reduced compared to the estimated oxygen
680 fugacity of the upper mantle (e.g., Cottrell and Kelley, 2011). These experiments were in
681 equilibrium with a MORB melt and yield values of $D_{Pb}^{\text{MSS/sulfide melt}} = 0.0049$ and 0.0052, with an
682 average value of 0.005 (Brenan, 2015). For comparison, Li and Audétat (2012, 2015) report
683 $D_{Pb}^{\text{MSS/sulfide melt}}$ ranging from 0.001 to 0.005 with an average of 0.003 for 16 experiments at a
684 range of oxygen fugacities, 1000–1250°C, and 0.5–2.5 GPa, and in equilibrium with melts
685 ranging in composition from hydrous basanite to rhyolite.

686 Results of our modeling (Fig. 10) indicate that >90% fractional crystallization is required
687 to produce an abyssal peridotite sulfide with 4 ppm Pb. The smaller the initial amount of Pb in
688 the model, the larger the amount of fractional crystallization needed to produce sulfides with 4
689 ppm Pb. When the sulfide melt initially contains 36 ppm Pb, 96% fractional crystallization is
690 needed, whereas an initial Pb content of 75 ppm requires only 91% fractional crystallization.
691 Hence, by assuming that all mantle Pb is initially in the sulfide melt, our model provides a lower
692 bound for the degree of fractional crystallization necessary to produce the average 4 ppm Pb
693 observed in sulfides from abyssal peridotites.

694 Our model predicts that sulfide melt contains 800 ppm Pb after crystallization of sulfide
695 with 4 ppm Pb. Such high concentrations have not been observed in peridotite or MORB sulfides

This is a preprint, the final version is subject to change, of the American Mineralogist (MSA)
Cite as Authors (Year) Title. American Mineralogist, in press.
DOI: https://doi.org/10.2138/am-2019-6516

and are not expected, given that Pb will transfer from sulfide melt to silicate melt as these melts rise through the mantle and the solubility of sulfur in silicate melt increases. Hence, the 800 ppm Pb left in sulfide melt after >90% fractional crystallization reflects the amount of Pb available to MORB from the sulfide portion of the mantle.

Reconciling Pb in peridotite sulfides with Pb in MORB

The evolution of Pb in sulfide melt as it travels upwards is complex, due to the increasing solubility of sulfur in silicate melt as pressure decreases (Mavrogenes and O'Neill, 1999; Smythe et al., 2017). This means that sulfide melt undergoes not just fractional crystallization after crossing its solidus, but also dissolution of sulfur into silicate melt as it ascends towards the surface. Thus, the Pb system is governed by $D_{Pb}^{\text{sulfide melt/silicate melt}}$ and the degree of sulfur saturation of the silicate melt, in addition to $D_{Pb}^{\text{sulfide/sulfide melt}}$ during fractional crystallization. In addition, partitioning of Pb in the sulfide melt-silicate melt system is complex due to its dependence on pressure, temperature, sulfide melt composition, and silicate melt composition (e.g., Hart and Gaetani, 2016; Kiseeva and Wood, 2013, 2015; Li and Audétat, 2015). Therefore, we do not directly model the evolution of the sulfide melt and silicate melt during upwelling beneath the ridge. Instead, we evaluate the implications of our modeled sulfide melt Pb contents for the Pb content of MORB.

In the previous section, we estimated that the average concentration of 4 ppm Pb in abyssal peridotite sulfides could be produced by >90% fractional crystallization, which results in sulfide melts with 800 ppm Pb. Our end-member model assumes that all mantle Pb was initially hosted in mantle sulfides, with an initial concentration of 36–75 ppm and a mode of 0.05%. Hence, after 90% fractional crystallization, sulfide melt will have a mode of 0.005%. If this

sulfide melt, which contains 800 ppm Pb, dissolves into silicate melt, then it will contribute 0.04 ppm to the MORB Pb budget. This value is an order of magnitude lower than the average of 0.6±0.4 ppm Pb measured in MORB glasses (Gale et al., 2013). If, as is more likely, less Pb is initially hosted in mantle sulfides, then the sulfide melt will still contain 800 ppm Pb after production of sulfides with 4 ppm Pb, but a larger amount of fractional crystallization will be necessary, leaving behind a smaller volume of sulfide melt.

Our calculations indicate that the systematics of the sulfide Pb budget do not allow sulfides to be the main host for mantle Pb prior to melting. The sulfide melt that remains after crystallization of sulfides with 4 ppm Pb contains an order of magnitude less Pb than is necessary to produce the amount of Pb in average MORB. Instead, the majority of mantle Pb is likely sequestered in silicate phases prior to the onset of melting, as previously suggested by Warren and Shirey (2012) and Zhang et al. (2018), with most Pb in MORB is derived from melting of the silicate mantle. In our calculations, we assumed that all mantle Pb was initially hosted in sulfide, which leads to a minimum estimate for the amount of fractional crystallization of the sulfide melt to produce the observed Pb concentrations in our sulfides. If most mantle Pb is instead hosted in silicate phases, then sulfides in abyssal peridotites must be the product of very high degrees (>>90%) of fractional crystallization and the amount of Pb-bearing sulfide melt remaining after this process is much smaller than our end-member estimates.

Se and Te in mantle sulfides

Among the other trace elements measured in this study, the elements Se and Te have received considerable attention as their siderophile/chalcophile behavior and relative volatility makes them tracers of processes such as core formation and subsequent addition of late-accreted

This is a preprint, the final version is subject to change, of the American Mineralogist (MSA)
Cite as Authors (Year) Title. American Mineralogist, in press.
DOI: https://doi.org/10.2138/am-2019-6516

material (e.g., Lorand et al., 2008; Morgan, 1986; Rose-Weston et al., 2009; Wang and Becker, 2013). Previous studies of abyssal peridotites, xenoliths, and primitive basalts have found that Se and Te are hosted in the mantle in base metal sulfides, with Te also occurring in telluride minerals and Pt-rich alloys (Guo et al., 1999; Hattori et al., 2002; Luguet et al., 2004; Lorand and Alard, 2010; König et al., 2012, 2014; Patten et al., 2013). Although concentrations of these two elements have been used to constrain primitive mantle composition and to trace early Earth accretion, sulfide melting and refertilization can also change Se/Te ratios (Lorand and Alard 2010; König et al. 2014, 2015; Lissner et al., 2014; Brenan 2015).

In this study, sulfides record a larger range of Te (<4–361 ppm) relative to Se (45–251 ppm) concentrations, as shown in Fig. 11A. The Se-Te concentration range in our sulfides is similar to other datasets for mantle sulfides (Guo et al., 1999; Hattori et al., 2002; Luguet et al., 2004; Lorand and Alard, 2010; König et al., 2014). This corresponds to a wide range in Se/Te ratios of 0.5– 56 (Table S4), also similar to previous studies (Fig. 11B), which have found large variations relative to the primitive mantle estimate of Se/Te = 8±2 (Wang and Becker, 2013).

As previously discussed, sulfides in this study are interpreted to be the result of complete melting at depths >250 km to form a sulfide melt, based on the experimental data of Zhang and Hirschmann (2016). At much shallower depths (~30 km) and lower temperatures (~1050–1200°C), based on the geotherm for slow spreading ridges (Fig. 8), fractional crystallization of this sulfide melt results in the crystallization of sulfide in peridotite. Trace element systematics in this system are governed by sulfide/sulfide melt partitioning, unlike the MORB system, where rapid quenching means that sulfide melt/silicate melt partitioning governs the trace element systematics.

This is a preprint, the final version is subject to change, of the American Mineralogist (MSA)
Cite as Authors (Year) Title. American Mineralogist, in press.
DOI: https://doi.org/10.2138/am-2019-6516

764 Experimental datasets (Helmy et al., 2007, 2010; Brenan, 2015) for partitioning between
765 sulfide and sulfide melt yield partition coefficients for Te ($D_{Te}^{MSS/sulfliq}$ = 0.02–0.065) that are an
766 order of magnitude lower than for Se ($D_{Se}^{MSS/sulfliq}$ = 0.6–0.7). Assuming the initial melting event
767 occurred under batch melting conditions and that this sulfide melt had a primitive mantle
768 composition (Se/Te=8±2, Te=11 ppb; Wang and Becker, 2013), then fractional crystallization of
769 sulfide from a sulfide melt will lead to sulfides with higher Se/Te ratios due to the greater
770 incompatibility of Te relative to Se (e.g., König et al., 2014; Brenan, 2015).
771 The low Se/Te ratios observed in many sulfides correspond to regions of these grains
772 with elevated Te abundances, whereas Se abundances are homogeneous across grains (Table S4).
773 This observation suggests the presence of discrete telluride micro- or nano-phases, similar to
774 those documented in orogenic peridotite sulfides (e.g., Luguet et al., 2004; Lorand et al., 2008,
775 2010). Experiments by Helmy et al. (2007, 2010) indicate that Te is highly incompatible in MSS
776 and that crystallization of discrete telluride phases occurs when telluride melt becomes
777 immiscible with sulfide melt at temperatures <1150°C. MORBs have high Se/Te ratios
778 (Hertogen et al., 1980; Lissner et al., 2014), consistent with the formation of Te-depleted melts
779 by crystallization of telluride phases in the mantle.
780

781 **IMPLICATIONS**

782 The trace element dataset for abyssal peridotite sulfides presented in this study provides
783 constraints on the role of mantle sulfides in the evolution of chalcophile and siderophile elements
784 in the Earth. Combined with previous studies, abyssal peridotite sulfides have a range of 0.1 to
785 36 ppm Pb and an average of 4 ppm Pb (n=136 grains). We created an end-member model for
786 sulfide petrogenesis to explore the implication of assuming that all mantle Pb is hosted in mantle

787 sulfides prior to melting. From this, we estimated that mantle sulfides contribute a maximum of
788 0.04 ppm Pb to MORB, which is an order of magnitude lower than the MORB average
789 concentration of 0.6±0.4 ppm Pb (Gale et al., 2013). Hence, while sulfides have been proposed
790 as a major control in the evolution of mantle Pb (e.g., Meijer et al., 1990; Hart and Gaetani,
791 2006), our results suggest that mantle sulfides cannot be the main host for mantle Pb, similar to
792 the conclusion reached in recent evaluations of the peridotite Pb budget (Warren and Shirey,
793 2012; Zhang et al., 2018). Instead, silicate phases must be an important host for mantle Pb and
794 better constraints are needed for the concentration range of Pb in these phases in peridotite.

795 The ability to collect in situ data on multiple trace elements in sulfides represents a
796 promising future avenue for refining models of their petrogenesis. The next generation of sulfide
797 models should be optimized to minimize the misfit between model and concentration data across
798 several elements, whereas this study focused on modeling Pb. Given the number of
799 unconstrained variables in the sulfide-silicate system, optimizing the fit of multiple elements
800 may provide a more robust constraint on the degree of melting and fractional crystallization
801 recorded by abyssal peridotite sulfides.

802 Finally, results from this study suggest that alteration leads to higher and more variable
803 concentrations of As, Sb, Ag, and Cl in sulfides, even in sulfides that otherwise appear unaltered.
804 Se, Te, and Au have similar concentrations among altered grains relative to unaltered grains and
805 show no intra-grain heterogeneity due to alteration, suggesting that these elements are relatively
806 fluid immobile during alteration. Pb shows behavior intermediate between these two groups of
807 elements, with elevated concentrations in altered sulfides, but minimal intra-grain heterogeneity,
808 suggesting that Pb is moderately susceptible to alteration. Given the importance of altered

oceanic lithosphere to subduction zone systems, trace element mapping would be a useful tool to provide improved constraints on the behavior of these elements during sulfide alteration.

ACKNOWLEDGEMENTS

We thank Jason Harvey, Sarah-Jane Barnes, James Brenan and Leslie Hayden for sharing reference materials in order to calibrate ion probe measurements. Discussions with Sarah-Jane Barnes, Ambre Luguet, John Lassiter, Suzanne Birner, Kathryn Kumamoto and Erik Hauri are greatly appreciated. Marty Grove is especially acknowledged for informal reviews of the paper and discussions of ion probe data quality. The Stanford-USGS Micro Analysis Center is thanked for instrument time, technical support, and scientific guidance. We are grateful to Kathy Barton for providing access to the SEM in her lab in the Department of Plant Biology at the Carnegie Institution for Science. We thank Dale Burns for measuring chlorine in sulfide by electron microprobe and Bob Jones for help with the electron microprobe measurements of sulfide major elements. Finally, we thank the David van Acken and an anonymous reviewer for comments that improved the manuscript and Kate Kiseeva for editorial handling. This study was partially supported by a National Science Foundation grant to JMW (OCE-1434199).

FIGURE CAPTIONS

Figure 1: Working curves for Pb measurements by SHRIMP-RG for all three sessions (D1-D3). **(A)** Measured $^{208}Pb/^{64}S_2$ versus accepted Pb concentration and calculated linear regression for the three reference materials. **(B)** Analytical precision based on the one-sigma standard deviation (i.e., reproducibility) of each reference material versus accepted Pb concentrations. Lower

831 concentration materials have greater error, due to increased scatter in counts near the detection
832 limit.
833
834 **Figure 2:** Representative images of pentlandite sulfides from abyssal peridotite samples. **(A)**
835 Reflected light photomicrograph and **(B)** layered EDS image of an interstitial pentlandite (Pn)
836 sulfide (PS59-235-18 sulfide 7) and surrounding olivine (Ol) and clinopyroxene (Cpx). **(C)**
837 Backscattered electron image of sample PS59-235-01 sulfide 1, showing a cluster of sulfides
838 within ~200 μm of each other. SHRIMP-RG pits are visible on the grain surfaces. **(D)** Reflected
839 light photomicrograph and **(E)** layered EDS image of sulfide associated with clinopyroxene and
840 spinel (Van7-85-49 sulfide 8A and 8B).
841
842 **Figure 3:** Images of Cu-bearing sulfides. **(A)** Reflected light photomicrograph and **(B)** Cu EDS
843 map of sulfide 1 from Van7-96-21V, which contains an isolated chalcopyrite (Ccp) phase
844 adjacent to Pn. **(C)** Reflected light photomicrograph and **(D)** Cu EDS map of sulfide 20 from
845 PS59-235-01, which contains Ccp distributed pervasively throughout the host Pn grain.
846 Reflected light photomicrograph **(E)** and Cu EDS map **(F)** of sulfide 15 from sample Van7-96-
847 28, which contains fine needles of Ccp in Pn.
848
849 **Figure 4:** Reflected light photomicrographs of altered sulfides. **(A)** Altered sulfide HLY0102-
850 70-75 sulfide 7A, showing iron hydroxide surrounding pentlandite. **(B)** Pseudo-euhedral
851 intergranular sulfide in sample PS59-201-39, which contains Cu-enriched vermicular patches,
852 based on EDS maps. This sulfide is interpreted as hydrothermal based on its euhedral
853 morphology, which Luguet et al. (2003) noted for grains of hydrothermal origin. **(C)** Sulfides

with mottled texture and dull coloring in sample Van7-85-49. **(D)** Sulfide with abundant cracks (Van7-96-28 sulfide 10A).

Figure 5: Average Pb concentrations in abyssal peridotite sulfides. **(A)** Pentlandite sulfides (blue circles), with the blue dashed line indicating the average Pb concentration of 2.9 ppm. **(B)** Altered sulfides (orange squares), with the orange dashed line indicating the average of these grains at 9.7 ppm. The detection limit varied by analytical session: 2.2 ppm for session D1, 2.0 ppm for session D2, and 2.3 ppm for session D3 (Table S3). The analytical error for individual points is 1-5 ppm, largely controlled by the lack of high-precision low concentration standards.

Figure 6: Pb concentrations in Cu-bearing sulfides for individual analytical spots. Diamonds denote analyses of Cu enriched regions of sulfides, while circles denote discrete Pn portions of the same sulfides. The vertical blue dashed line at 2.9 ppm Pb is the average composition of all Pn grains in this study, while the green dashed line at 7.9 ppm Pb is the average of all Cu-bearing sulfides. The detection limit varied by analytical session: 2.2 ppm for session D1, 2.0 ppm for session D2, and 2.3 ppm for session D3 (Table S3). The analytical error for individual points is 1-5 ppm, largely controlled by the lack of high-precision low concentration standards. Grains labeled in turquoise have intra-grain Pb heterogeneity resolvable outside of analytical precision.

Figure 7: Trace element concentrations averaged by grain for Se, Te, As, Sb, Ag, and Au in Pn and Cu-bearing sulfides (where "Cu-dist." corresponds to grains with distributed Cu enrichments as shown in Fig. 3). Vertical dashed lines are the average concentration of each element for all Pn (blue) and Cu-bearing (green) sulfides. The concentration scale for Au is three orders of

magnitude less than for all other elements. The detection limit (D.L.) is shown for Se (6.5 ppm) and As (5 ppm during session C1 and 1.5 ppm during session C2; Table S4). The detection limit falls below the lower limit of the plot for Te (0.5 ppm), Sb (0.08 ppm), and Ag (0.7 ppm). The detection limit is not known for Au, as discussed in the Supplemental Methods. Grains are compositionally heterogeneous for most elements, except Se and Au, and the averages for many grains are underlain by 1-3 orders of magnitude range in concentration (see Table S4 for individual analyses).

Figure 8: Schematic model for sulfide petrogenesis. **(A)** Pressure-temperature diagram for mantle melting, showing the MSS solidus and liquidus relative to the anhydrous and hydrous peridotite solidi (adapted from Zhang and Hirschmann, 2016). The mantle adiabat is for a mantle potential temperature of 1350°C and the oceanic geotherm is for an ultra-slow spreading ridge (adapted from Birner et al., 2018). The depth conversion for pressure is based on the approximation for mantle lithologies that 1 GPa ≈ 30 km. **(B)** MSS undergoes complete batch melting to sulfide melt during mantle upwelling, prior to the formation of any silicate melt. This occurs at depths ≥ 250 km, based on the MSS melting experiments of Zhang and Hirschmann (2016). **(C)** At shallow depths (<30 km), sulfide melt undergoes fractional crystallization to produce sulfide (Pn ± Ccp) as the lithospheric mantle cools prior to emplacement on the seafloor.

Figure 9: Compilation of sulfide Pb in mid-ocean ridge peridotites and basalts, showing concentrations of individual unaltered grains. Sulfide measurements in this study are by SHRIMP, whereas datasets from Warren and Shirey (2012) and Burton et al. (2012) are by TIMS, which has a lower detection limit. Ridge average concentrations are calculated from grain

averages (not averages of all individual points) and combine both pentlandite and Cu-bearing grains. Shown for comparison are the Pb concentrations in individual MORB sulfides (Patten et al., 2013) and the average of normal MORB glass (Gale et al., 2013; the 95% confidence limit is smaller than the symbol).

Figure 10: Model for the evolution of Pb in mantle sulfides formed by fractional crystallization of a sulfide melt. The model was run using three different estimates for initial mantle Pb content (Salters and Stracke, 2004; Workman and Hart, 2005; Hart and Gaetani, 2006) and a sulfide/sulfide melt partition coefficient of 0.005 (Brenan, 2015). The resulting sulfide (C_S) is shown as solid lines, while the sulfide melt (C_L) is shown as dashed lines. The solid black line corresponds to the average Pb concentration of 4 ppm in all unaltered abyssal peridotite sulfides (Fig. 9), while the shaded grey field corresponds to their range of 0.1–36 ppm. Our model suggests that abyssal peridotite sulfides are formed, on average, by >90% fractional crystallization.

Figure 11: Variations in mantle sulfide on an individual analysis basis for **(A)** Se versus Te and **(B)** Se/Te versus Te. Pentlandite (circles) and Cu-bearing sulfides (diamonds) from this study are compared to previous studies of sulfides in peridotite xenoliths (Guo et al., 1999; Hattori et al., 2002), orogenic peridotites (Lorand and Alard, 2010; König et al., 2014) and an ophiolite (Luguet et al., 2004). The estimated primitive mantle (PM) value from Wang and Becker (2013) is shown as a star. Se/Te ratios higher than PM are best explained by fractional crystallization of sulfide from a sulfide melt, as $D_{Se}^{MSS/sulfliq} > D_{Te}^{MSS/sulfliq}$ (Helmy et al., 2007, 2010; Brenan, 2015). Low Se/Te ratios suggest Te enrichment due to the formation of telluride micro- or nano-

phases, as has been observed in other peridotite massifs (Luguet et al., 2004; Lorand et al., 2008, 2010).

REFERENCES

Alard, O., Griffin, W.L., Lorand, J.-P., Jackson, S.E., and O'Reilly, S.Y. (2000) Non-chondritic distribution of the highly siderophile elements in mantle sulphides. Nature, 407, 891–894.

Alard, O., W.L. Griffin, Pearson, N.J., Lorand, J.-P., and O'Reilly, S.Y. (2002) New insights into the Re–Os systematics of sub-continental lithospheric mantle from in situ analysis of sulphides. Earth and Planetary Science Letters, 203, 651–663.

Alard, O., Luguet, A., Pearson, N.J., Griffin, W.L., Lorand, J.P., Gannoun, A., Burton, K.W., and O'Reilly, S.Y. (2005) In situ Os isotopes in abyssal peridotites bridge the isotopic gap between MORBs and their source mantle. Nature, 436, 1005–1008.

Alard, O., Lorand, J.-P., Reisberg, L., Bodinier, J.-L., Dautria, J.-M., and O'Reilly, S.Y. (2011) Volatile-rich Metasomatism in Montferrier Xenoliths (Southern France): Implications for the Abundances of Chalcophile and Highly Siderophile Elements in the Subcontinental Mantle. Journal of Petrology, 52, 2009–2045.

Alt, J.C., and Shanks, W. (2003) Serpentinization of abyssal peridotites from the MARK area , Mid-Atlantic Ridge: Sulfur geochemistry and reaction modeling. Geochimica et Cosmochimica Acta, 67, 641–653.

Ariskin, A. A., Danyushevsky, L.V., Bychkov, K.A., McNeill, A.W., Barmina, G.S., and Nikolaev, G.S. (2013) Modeling solubility of Fe-Ni sulfides in basaltic magmas: the effect of nickel. Economic Geology, 108, 1983–2003.

946 Bach, W., and Früh-Green, G.L. (2010) Alteration of the oceanic lithosphere and implications
947 for seafloor processes. Elements, 6, 173–178.
948 Bach, W., Peucker-Ehrenbrink, B., Hart, S.R., and Blusztajn, J.S. (2003) Geochemistry of
949 hydrothermally altered oceanic crust: DSDP/ODP Hole 504B – Implications for seawater-
950 crust exchange budgets and Sr- and Pb-isotopic evolution of the mantle. Geochemistry
951 Geophysics Geosystems, 4, 8904.
952 Barnes, S.J., Makovicky, E., Makovicky, M., Rose-Hansen, J., and Karup-Moller, S. (1997)
953 Partition coefficients for Ni, Cu, Pd, Pt, Rh, and Ir between monosulfide solid solution and
954 sulfide liquid and the formation of compositionally zoned Ni-Cu sulfide bodies by fractional
955 crystallization of sulfide liquid. Canadian Journal of Earth Sciences, 34, 366–374.
956 Birner, S. K., Cottrell, E., Warren, J.M., Kelley, K.A., and Davis, F.A. (2018) Peridotites and
957 basalts reveal broad congruence between two independent records of mantle fO2 despite
958 local redox heterogeneity. Earth and Planetary Science Letters, 494, 172–189.
959 Blusztajn, J., Shimizu, N., Warren, J.M., and Dick, H.J.B. (2014) In-situ Pb isotopic analysis of
960 sulfides in abyssal peridotites: New insights into heterogeneity and evolution of the oceanic
961 upper mantle. Geology, 42, 159–162.
962 Bockrath, C., Ballhaus, C., and Holzheid, A. (2004) Fractionation of the platinum-group
963 elements during mantle melting. Science, 305, 1951–1953.
964 Brenan, J.M. (2015) Se-Te fractionation by sulfide-silicate melt partitioning: Implications for the
965 composition of mantle-derived magmas and their melting residues. Earth and Planetary
966 Science Letters, 422, 45–57.

967 Bulanova, G.P., Griffin, W.L., Ryan, C.G., Shestakova, O.Y., and Barnes, S.-J. (1996) Trace
968 elements in sulfide inclusions from Yakutian diamonds. Contributions to Mineralogy and
969 Petrology, 124, 111–125.
970 Burton, K.W., Cenki-Tok, B., Mokadem, F., Harvey, J., Gannoun, A., Alard, O., and Parkinson,
971 I.J. (2012) Unradiogenic lead in Earth's upper mantle. Nature Geoscience, 5, 1–4.
972 Czamanske, G.K., and Moore, J.G. (1977) Composition and phase chemistry of sulfide globules
973 in basalt from the Mid-Atlantic Ridge rift valley near 37°N lat. Bulletin of the Geological
974 Society of America, 88, 587–599.
975 D'Errico, M.E., Warren, J.M., and Godard, M. (2016) Evidence for chemically heterogeneous
976 Arctic mantle beneath the Gakkel Ridge. Geochimica et Cosmochimica Acta, 174, 291–312.
977 Dare, S.A.S., Barnes, S.J., and Prichard, H.M. (2010) The distribution of platinum group
978 elements (PGE) and other chalcophile elements among sulfides from the Creighton Ni-Cu-
979 PGE sulfide deposit, Sudbury, Canada, and the origin of palladium in pentlandite.
980 Mineralium Deposita, 45, 765–793.
981 Dare, S.A.S., Barnes, S.J., Prichard, H.M., and Fisher, P.C. (2011) Chalcophile and platinum-
982 group element (PGE) concentrations in the sulfide minerals from the McCreedy East
983 deposit, Sudbury, Canada, and the origin of PGE in pyrite. Mineralium Deposita, 46, 381–
984 407.
985 Dick, H.J.B., Lin, J., and Schouten, H. (2003) An ultraslow-spreading class of ocean ridge.
986 Nature, 426, 405–412.
987 Duran, C.J., Barnes, S.-J., and Corkery, J.T. (2016) Chalcophile and platinum-group element
988 distribution in pyrites from the sulfide-rich pods of the Lac des Iles Pd deposits, Western

989 Ontario, Canada: Implications for post-cumulus re-equilibration of the ore and the use of
990 pyrite compositions in exploration. Journal of Geochemical Exploration, 158, 223–242.
991 Eldridge, C.S., Compston, W., Williams, I.S., Harris, J.W., and Bristow, J.W. (1991) Isotope
992 evidence for the involvement of recycled sediments in diamond formation. Nature, 353,
993 649–653.
994 Fleet, M.E. (2006) Phase Equilibria at High Temperatures. Reviews in Mineralogy and
995 Geochemistry, 61, 365–419.
996 Francis, R.D. (1990) Sulfide globules in mid-ocean ridge basalts (MORB), and the effect of
997 oxygen abundance in FeSO liquids on the ability of those liquids to partition metals from
998 MORB and komatiite magmas. Chemical Geology, 85, 199–213.
999 Gale, A., Dalton, C.A., Langmuir, C.H., Su, Y., and Schilling, J.-G. (2013) The mean
1000 composition of ocean ridge basalts. Geochemistry, Geophysics, Geosystems, 14, 489–518.
1001 Gast, P.W. (1968) Trace element fractionation and the origin of tholeiitic and alkaline magma
1002 types. Geochimica et Cosmochimica Acta, 32, 1057–1086.
1003 Godard, M., Bosch, D., and Einaudi, F. (2006) A MORB source for low-Ti magmatism in the
1004 Semail ophiolite. Chemical Geology, 234, 58–78.
1005 Guo, J., Griffin, W.L., and O'Reilly, S.Y. (1999) Geochemistry and Origin of Sulphide Minerals
1006 in Mantle Xenoliths: Qilin, Southeastern China. Journal of Petrology, 40, 1125–1149.
1007 Hart, S.R., and Gaetani, G.A. (2006) Mantle Pb paradoxes: the sulfide solution. Contributions to
1008 Mineralogy and Petrology, 152, 295–308.
1009 Hart, S.R., and Gaetani, G.A. (2016) Experimental determination of Pb partitioning between
1010 sulfide melt and basalt melt as a function of P, T and X. Geochimica et Cosmochimica Acta,
1011 185, 9–20.

1012 Harvey, J., Dale, C.W., Gannoun, A., and Burton, K.W. (2011) Osmium mass balance in
1013 peridotite and the effects of mantle-derived sulphides on basalt petrogenesis. Geochimica et
1014 Cosmochimica Acta, 75, 5574–5596.
1015 Harvey, J., Warren, J.M., and Shirey, S.B. (2016) Mantle Sulfides and their role in Re-Os and Pb
1016 isotope Geochronology. Reviews in Mineralogy & Geochemistry, 81, 579–649.
1017 Hattori, K.H., Arai, S., and Clarke Barrie, D.B. (2002) Selenium, tellurium, arsenic and
1018 antimony contents of primary mantle sulfides. Canadian Mineralogist, 40, 637–650.
1019 Hayden, L.A., Van Orman, J.A., McDonough, W.F., Ash, R.D., and Goodrich, C.A. (2011)
1020 Trace element partitioning in the Fe-S-C system and its implications for planetary
1021 differentiation and the thermal history of ureilites. Geochimica et Cosmochimica Acta, 75,
1022 6570–6583.
1023 Hellebrand, E., Snow, J.E., Mostefaoui, S., and Hoppe, P. (2005) Trace element distribution
1024 between orthopyroxene and clinopyroxene in peridotites from the Gakkel Ridge: a SIMS
1025 and NanoSIMS study. Contributions to Mineralogy and Petrology, 150, 486–504.
1026 Helmy, H.M., Ballhaus, C., Berndt, J., Bockrath, C., and Wohlgemuth-Ueberwasser, C.C. (2007)
1027 Formation of Pt, Pd and Ni tellurides: experiments in sulfide–telluride systems.
1028 Contributions to Mineralogy and Petrology, 153, 577–591.
1029 Helmy, H.M., Ballhaus, C., Wohlgemuth-Ueberwasser, C.C., Fonseca, R.O.C., and Laurenz, V.
1030 (2010) Partitioning of Se, As, Sb, Te and Bi between monosulfide solid solution and sulfide
1031 melt - Application to magmatic sulfide deposits. Geochimica et Cosmochimica Acta, 74,
1032 6174–6179.

1033 Holzheid, A., Schmitz, M.D., and Grove, T.L. (2000) Textural equilibria of iron sulfide liquids in
1034 partly molten silicate aggregates and their relevance to core formation scenarios. Journal of
1035 Geophysical Research, 105, 1355–13567.
1036 Holzheid, A., and Grove, T.L. (2002), Sulfur saturation limits in silicate melts and their
1037 implications for core formation scenarios for terrestrial planets, American Mineralogist, 87,
1038 227–237.
1039 Jagoutz, E., Palme, H., Baddenhausen, H., Blum, K., Cendales, M., Dreibus, G., Spettel, B.,
1040 Lorenz, V., and Wanke, H. (1979) The abundances of major, minor and trace elements in
1041 the Earth's mantle as derived from primitive ultramafic nodules. 10^{th} Lunar and Planetary
1042 Science Conference, 2031–2050.
1043 Jokat, W., Ritzmann, O., Schmidt-Aursch, M.C., Drachev, S., Gauger, S., and Snow, J. (2003)
1044 Geophysical evidence for reduced melt production on the Arctic ultraslow Gakkel mid-
1045 ocean ridge. Nature, 423, 962–5.
1046 Kadko, D., Koski, R., Tatsumoto, M., and Bouse, R. (1985) An estimate of hydrothermal fluid
1047 residence times and vent chimney growth rates based on ^{210}Pb/Pb ratios and mineralogic
1048 studies of sulfides dredged from the Juan de Fuca Ridge. Earth and Planetary Science
1049 Letters, 76, 35–44.
1050 Kiseeva, E.S., and Wood, B.J. (2013) A simple model for chalcophile element partitioning
1051 between sulphide and silicate liquids with geochemical applications. Earth and Planetary
1052 Science Letters, 383, 68–81.
1053 Kiseeva, E.S., and Wood, B.J. (2015) The effects of composition and temperature on chalcophile
1054 and lithophile element partitioning into magmatic sulphides. Earth and Planetary Science
1055 Letters, 424, 280–294.

1056 Klein, F., and Bach, W. (2009) Fe-Ni-Co-O-S Phase Relations in Peridotite-Seawater
1057 Interactions. Journal of Petrology, 50, 37–59.
1058 Klein, F., Humphris, S.E., Guo, W., Schubotz, F., Schwarzenbach, E.M., and Orsi, W.D. (2015)
1059 Fluid mixing and the deep biosphere of a fossil Lost City-type hydrothermal system at the
1060 Iberia Margin. Proceedings of the National Academy of Sciences, 112, 12036–12041.
1061 König, S., Luguet, A., Lorand, J.-P., Wombacher, F., and Lissner, M. (2012) Selenium and
1062 tellurium systematics of the Earth's mantle from high precision analyses of ultra-depleted
1063 orogenic peridotites. Geochimica et Cosmochimica Acta, 86, 354–366.
1064 König, S., Lorand, J.-P., Luguet, A., and Graham Pearson, D. (2014) A non-primitive origin of
1065 near-chondritic S-Se-Te ratios in mantle peridotites; implications for the Earth's late
1066 accretionary history. Earth and Planetary Science Letters, 385, 110–121.
1067 König, S., Lissner, M., Lorand, J.-P., Bragagni, A., and Luguet, A. (2015) Mineralogical control
1068 of selenium, tellurium and highly siderophile elements in the Earth's mantle: Evidence from
1069 mineral separates of ultra-depleted mantle residues. Chemical Geology, 396, 16–24.
1070 Kullerud, G., Yund, R.A., and Moh, G.H. (1969) Phase Relations in the Cu-Fe-S, Cu-Ni-S, and
1071 Fe-Ni-S Systems. Economic Geology Monograph, 4, 323–343.
1072 Li, Y. (2014) Chalcophile element partitioning between sulfide phases and hydrous mantle melt:
1073 Applications to mantle melting and the formation of ore deposits. Journal of Asian Earth
1074 Sciences, 94, 77–93.
1075 Li, Y., and Audétat, A. (2012) Partitioning of V, Mn, Co, Ni, Cu, Zn, As, Mo, Ag, Sn, Sb, W,
1076 Au, Pb, and Bi between sulfide phases and hydrous basanite melt at upper mantle
1077 conditions. Earth and Planetary Science Letters, 355–356, 327–340.

1078 Li, Y., and Audétat, A. (2015) Effects of temperature, silicate melt composition, and oxygen
1079 fugacity on the partitioning of V, Mn, Co, Ni, Cu, Zn, As, Mo, Ag, Sn, Sb, W, Au, Pb, and
1080 Bi between sulfide phases and silicate melt. Geochimica et Cosmochimica Acta, 162, 25–
1081 45.
1082 Lissner, M., König, S., Luguet, A., le Roux, P.J., Schuth, S., Heuser, A., and le Roex, A.P.
1083 (2014) Selenium and tellurium systematics in MORBs from the southern Mid-Atlantic
1084 Ridge (47-50°S). Geochimica et Cosmochimica Acta, 144, 379–402.
1085 Liu, C.Z., Snow, J.E., Brügmann, G., Hellebrand, E., and Hofmann, A.W. (2009) Non-chondritic
1086 HSE budget in Earth's upper mantle evidenced by abyssal peridotites from Gakkel ridge
1087 (Arctic Ocean). Earth and Planetary Science Letters, 283, 122–132.
1088 Lorand, J.-P. (1990) Are spinel lherzolite xenoliths representative of the abundance of sulfur in
1089 the upper mantle? Geochimica et Cosmochimica Acta, 54, 1487–1492.
1090 Lorand, J.-P., and Alard, O. (2001) Platinum-group element abundances in the upper mantle:
1091 New constraints from in situ and whole-rock analyses of massif central xenoliths (France).
1092 Geochimica et Cosmochimica Acta, 65, 2789–2806.
1093 Lorand, J.-P., and Luguet, A. (2016) Chalcophile and Siderophile Elements in Mantle Rocks:
1094 Trace Elements Controlled By Trace Minerals. Reviews in Mineralogy and Geochemistry,
1095 81, 441–488.
1096 Lorand, J.-P., Reisberg, L., and Bedini, R.M. (2003) Platinum-group elements and melt
1097 percolation processes in Sidamo spinel peridotite xenoliths, Ethiopia, East African Rift.
1098 Chemical Geology, 196, 57–75.

1099 Lorand, J.-P., Delpech, G., Grégoire, M., Moine, B.N., O'Reilly, S.Y., and Cottin, J.-Y. (2004)
1100 Platinum-group elements and the multistage metasomatic history of Kerguelen lithospheric
1101 mantle (South Indian Ocean). Chemical Geology, 208, 195–215.
1102 Lorand, J.-P., Luguet, A., Alard, O., Bezos, A., and Meisel, T. (2008) Abundance and
1103 distribution of platinum-group elements in orogenic lherzolites; a case study in a Fontete
1104 Rouge lherzolite (French Pyrénées). Chemical Geology, 248, 174–194.
1105 Lorand, J.-P., and Alard, O. (2010) Determination of selenium and tellurium concentrations in
1106 Pyrenean peridotites (Ariege, France): New insight into S/Se/Te systematics of the upper in
1107 mantle samples. Chemical Geology, 278, 120–130.
1108 Lorand, J.-P., Alard, O., and Luguet, A. (2010) Platinum-group element micronuggets and
1109 refertilization process in Lherz orogenic peridotite (northeastern Pyrenees, France), Earth
1110 and Planetary Science Letters, 289, 298–310.
1111 Luguet, A., and Reisberg, L. (2016) Highly Siderophile Element and ^{187}Os Signatures in Non-
1112 cratonic Basalt-hosted Peridotite Xenoliths: Unravelling the Origin and Evolution of the
1113 Post-Archean Lithospheric Mantle. Reviews in Mineralogy and Geochemistry, 81, 305–367.
1114 Luguet, A., Alard, O., Lorand, J.-P., Pearson, N.J., Ryan, C.G., and O'Reilly, S.Y. (2001) Laser-
1115 ablation microprobe (LAM)-ICPMS unravels the highly siderophile element geochemistry
1116 of the oceanic mantle. Earth and Planetary Science Letters, 189, 285–294.
1117 Luguet, A., Lorand, J.-P., and Seyler, M. (2003) Sulfide petrology and highly siderophile
1118 element geochemistry of abyssal peridotites: a coupled study of samples from the Kane
1119 Fracture Zone (45°W 23°20N, MARK area, Atlantic Ocean). Geochimica et Cosmochimica
1120 Acta, 67, 1553–1570.

1121 Luguet, A., Lorand, J.-P., Alard, O., and Cottin, J.Y. (2004) A multi-technique study of platinum
1122 group element systematic in some Ligurian ophiolitic peridotites, Italy. Chemical Geology,
1123 208, 175–194.
1124 Mathez, E.A. (1976) Sulfur solubility and magmatic sulfides in submarine basalt glass. Journal
1125 of Geophysical Research, 81, 4269–4276.
1126 Mavrogenes, J.A., and O'Neill, H.S.C. (1999) The relative effects of pressure, temperature and
1127 oxygen fugacity on the solubility of sulfide in mafic magmas. Geochimica et Cosmochimica
1128 Acta, 63, 1173–1180.
1129 Meijer, A., Kwon, T., and Tilton, G.R. (1990) U-Th-Pb Partitioning Behavior During Partial
1130 Melting in the Upper Mantle: Implications for the Origin of High Mu Components and the
1131 "Pb Paradox." Journal of Geophysical Research, 95, 433–448.
1132 Metz, S., and Trefry, J.H. (2000) Chemical and mineralogical influences on concentrations of
1133 trace metals in hydrothermal fluids. Geochimica et Cosmochimica Acta, 64, 2267–2279.
1134 Michael, P.J., Langmuir, C.H., Dick, H.J.B., and Snow, J.E. (2003) Magmatic and amagmatic
1135 seafloor generation at the ultraslow-spreading Gakkel ridge, Arctic Ocean. Nature, 423,
1136 956–961.
1137 Morgan, J.W., Wandless, G.A., Petrie, R.K., and Irving, A.J. (1981) Composition of the earth's
1138 upper mantle - I. Siderophile trace elements in ultramafic nodules. Tectonophysics, 75, 47–
1139 67.
1140 Morgan, J.W. (1986) Ultramafic Xenoliths: Clues to Earth's Late Accretionary History. Journal
1141 of Geophysical Research, 91, 12375–12387.

1142 Morgan, J.W., Walker, R.J., Brandon, A.D., and Horan, M.F. (2001) Siderophile elements in
1143 Earth's upper mantle and lunar breccias: Data synthesis suggests manifestations of the same
1144 late influx. Meteoritics and Planetary Science, 36, 1257–1275.
1145 Naldrett, A.J., Innes, D.G., Sowa, J., and Gorton, M.P. (1982) Compositional variations within
1146 and between five Sudbury ore deposits. Economic Geology, 77, 1519–1534.
1147 Niu, Y. (2004) Bulk-rock major and trace element compositions of abyssal peridotites:
1148 Implications for mantle melting, melt extraction and post-melting processes beneath mid-
1149 ocean ridges. Journal of Petrology, 45, 2423–2458.
1150 Norman, M., Robinson, P., and Clark, D. (2003) Major- and trace-element analysis of sulfide
1151 ores by laser-ablation ICP-MS, solution ICP-MS, and XRF: New data on international
1152 reference materials. Canadian Mineralogist, 41, 293–305.
1153 Patten, C.G.C., Barnes, S.-J., and Mathez, E.A. (2012) Textural variations in MORB sulfide
1154 droplets due to differences in crystallization history. Canadian Mineralogist, 50, 675–692.
1155 Patten, C.G.C., Barnes, S.-J., Mathez, E.A., and Jenner, F.E. (2013) Partition coefficients of
1156 chalcophile elements between sulfide and silicate melts and the early crystallization history
1157 of sulfide liquid: LA-ICP-MS analysis of MORB sulfide droplets. Chemical Geology, 358,
1158 170–188.
1159 Paulick, H., Bach, W., Godard, M., De Hoog, J.C.M., Suhr, G., and Harvey, J. (2006)
1160 Geochemistry of abyssal peridotites (Mid-Atlantic Ridge, 15°20′N, ODP Leg 209):
1161 Implications for fluid/rock interaction in slow spreading environments. Chemical Geology,
1162 234, 179–210.
1163 Pearson, D.G., and Shirey, S.B. (1999) Isotopic dating of diamonds. Reviews in Economic
1164 Geology, 12, 143–172.

1165 Pearson, D.G., Parman, S.W., and Nowell, G.M. (2007) A link between large mantle melting
1166 events and continent growth seen in osmium isotopes. Nature, 449, 202–205.
1167 Peregoedova, A., and Ohnenstetter, M. (2002) Collectors of Pt, Pd and Rh in a S-poor Fe-Ni-Cu
1168 sulfide system at 760°C: Experimental data and application to ore deposits. Canadian
1169 Mineralogist, 40, 527–561.
1170 Regelous, M., Weinzierl, C.G., and Haase, K.M. (2016) Controls on melting at spreading ridges
1171 from correlated abyssal peridotite – mid-ocean ridge basalt compositions. Earth and
1172 Planetary Science Letters, 449, 1–11.
1173 Rose-Weston, L., Brenan, J.M., Fei, Y., Secco, R.A., and Frost, D.J. (2009) Effect of pressure,
1174 temperature, and oxygen fugacity on the metal-silicate partitioning of Te, Se, and S:
1175 Implications for earth differentiation. Geochimica et Cosmochimica Acta, 73, 4598–4615.
1176 Rudnick, R.L., Eldridge, C.S., and Bulanova, G.P. (1993) Diamond growth history from in situ
1177 measurement of Pb and S isotopic compositions of sulfide inclusions. Geology, 21, 13–16.
1178 Saal, A.E., Hauri, E.H., Langmuir, C.H., and Perfit, M.R. (2002) Vapour undersaturation in
1179 primitive mid-ocean-ridge basalt and the volatile content of Earth's upper mantle. Nature,
1180 419, 451-455.
1181 Salters, V.J.M., and Stracke, A. (2004) Composition of the depleted mantle. Geochemistry,
1182 Geophysics, Geosystems, 5, 1–27.
1183 Schmidt, K., Koschinsky, A., Garbe-Schonberg, D., de Carvalho, L.M., and Seifert, R. (2007)
1184 Geochemistry of hydrothermal fluids from the ultramafic-hosted Logatchev hydrothermal
1185 field, 15°N on the Mid-Atlantic Ridge: Temporal and spatial investigation. Chemical
1186 Geology, 242, 1–21.

1187 Shaw, D.M. (1970) Trace element fractionation during anatexis. Geochimica et Cosmochimica
1188 Acta, 34, 237–243.
1189 Shimazaki, H., and MacLean, W.H. (1976) An experimental study on the partition of zinc and
1190 lead between the silicate and sulfide liquids. Mineralium Deposita, 11, 125–132.
1191 Shirey, S.B., and Shigley, E. (2013) Recent advances in understanding the geology of diamonds.
1192 Gems and Gemology, 49, 188–22.
1193 Smythe, D.J., Wood, B.J., and Kiseeva, E.S. (2017) The S content of silicate melts at sulfide
1194 saturation: new experiments and a model incorporating the effects of sulfide composition.
1195 American Mineralogist, 102, 795–803.
1196 Standish, J.J., Dick, H.J.B., Michael, P.J., Melson, W.G., and O'Hearn, T. (2008) MORB
1197 generation beneath the ultraslow spreading Southwest Indian Ridge (9–25°E): Major
1198 element chemistry and the importance of process versus source. Geochemistry Geophysics
1199 Geosystems, 9, Q05004.
1200 Szabó, C., and Bodnar, R.J. (1995) Chemistry and origin of mantle sulfides in spinel peridotite
1201 xenoliths from alkaline basaltic lavas, Nógrád-Gömör Volcanic Field, northern Hungary
1202 and southern Slovakia, Geochimica et Cosmochimica Acta, 59, 3917–3927.
1203 Tatsumoto, M., and Patterson, C.C. (1963) Concentrations of common lead in some Atlantic and
1204 Mediterranean waters and in snow. Nature, 199, 350–352.
1205 Tivey, M.K. (2007) Generation of Seafloor Hydrothermal Vent Fluids and Associated Mineral
1206 Deposits. Oceanography, 20, 50–65.
1207 Tivey, M.K., Humphris, S.E., Thompson, G., Hannington, M.D., and Rona, P.A. (1995)
1208 Deducing patterns of fluid flow and mixing within the TAG active hydrothermal mound

using mineralogical and geochemical data. Journal of Geophysical Research, 100, 12527–12555.

Tsuno, K., and Dasgupta, R. (2015) Fe-Ni-Cu-C-S phase relations at high pressures and temperatures – The role of sulfur in carbon storage and diamond stability at mid- to deep-upper mantle. Earth and Planetary Science Letters, 412, 132–142.

Walker, R.J. (2016) Siderophile Elements in Tracing Planetary Formation and Evolution. Geochemical Perspectives, 5, 1–151.

Wang, Z., and Becker, H. (2013) Ratios of S, Se and Te in the silicate Earth require a volatile-rich late veneer. Nature, 499, 328–331.

Wang, Z., Lazarov, M., Steinmann, L.K., Becker, H., Zou, Z., and Geng, X.-L. (2018) The distribution of lead and thallium in mantle rocks: Insights from the Balmuccia peridotite massif (Italian Alps). American Mineralogist, 103, 1185–1199.

Warren, J.M. (2016) Global Variations in Abyssal Peridotite Compositions. Lithos, 248–251, 193–219.

Warren, J.M., and Shirey, S.B. (2012) Lead and osmium isotopic constraints on the oceanic mantle from single abyssal peridotite sulfides. Earth and Planetary Science Letters, 359–360, 279–293.

Warren, J.M., Shimizu, N., Sakaguchi, C., Dick, H.J.B., and Nakamura, E. (2009) An assessment of upper mantle heterogeneity based on abyssal peridotite isotopic compositions. Journal of Geophysical Research, 114, 1–36.

Wilson, R.G. (1995) SIMS quantification in Si, GaAs, and diamond - an update. Internaional Journal of Mass Spectrometry and Ion Processes, 143, 43–49.

1231 Workman, R.K., and Hart, S.R. (2005) Major and trace element composition of the depleted
1232 MORB mantle (DMM). Earth and Planetary Science Letters, 231, 53–72.
1233 Yang, A.Y., Zhou, M.-F., Zhao, T.-P., Deng, X.-G., Qi. L., and Xu, J.-F. (2014) Chalcophile
1234 elemental compositions of MORBs from the ultraslow-spreading Southwest Indian Ridge
1235 and controls of lithospheric structure on S-saturated differentiation. Chemical Geology, 382,
1236 1–13.
1237 Zhang, Z., and Hirschmann, M.M. (2016) Experimental constraints on mantle sulfide melting up
1238 to 8 GPa. American Mineralogist, 101, 181–192.

This is a preprint, the final version is subject to change, of the American Mineralogist (MSA)
Cite as Authors (Year) Title. American Mineralogist, in press.
DOI: https://doi.org/10.2138/am-2019-6516

Table 1. Sample locations and lithologies analyzed on SHRIMP-RG

		Location						Analytica
Dredge	Sample	Zone	Latitude	Longitude	Depth (m)	Lithology	Mount name[a]	O_2^- beam[b]
Gakkel Ridge								
HLY0102-70	62	EVZ	86.7500	64.7242	-4129	Harzburgite	70-62MountE	D3
HLY0102-70	75	EVZ	86.7500	64.7242	-4129	Lherzolite	MountB-TS	D2
PS59-201	39	SMZ	85.4908	16.9983	-3013	Harzburgite	MountB-TS	D2
PS59-235	01	SMZ	84.6392	4.2150	-3801	Lherzolite	235-01TS, 235-01MountA	D1, D2
PS59-235	17	SMZ	84.6392	4.2150	-3801	Lherzolite	MountC-TS	D3
PS59-235	18	SMZ	84.6392	4.2150	-3801	Lherzolite	235-18TS	D2
PS59-238	75	SMZ	84.7900	5.6783	-3797	Lherzolite	MountB-TS	D2
Southwest Indian Ridge								
Van7-85	47	Oblique	-52.2533	15.2325	4190	Lherzolite	MountD-TS	D3
Van7-85	49	Oblique	-52.2533	15.2325	4190	Lherzolite	MountD-TS	D3
Van7-96	21M[d]	Oblique	-53.1407	9.9792	3134	Harzburgite with vein[d]	96-21TS	D3
Van7-96	21V[d]	Oblique	-53.1407	9.9792	3134	Vein in harzburgite[d]	96-21TS	D3
Van7-96	28	Oblique	-53.1407	9.9792	3134	Lherzolite	MountC-TS	D3

a. Suffix "TS" indicates mount made from pieces cut from thin sections. All other mounts made from polished rock chips.

b. O_2^- primary ion beam was used to measure Pb concentrations in sessions D1-D3.

c. Cs^+ primary ion beam was used to measure Cl, As, Se, Sb, Te, Ag, and Au concentrations in session C1 and C2. Only Mo measured in session C1. The abbreviation "n.a." indicates that a mount was not analyzed. Fewer sulfides were measured dur sessions than the O2- sessions due to limited analytical time.

d. Suffix "M" refers to peridotite matrix and suffix "V" refers to vein. Sample is a plagioclase harzburgite with a plagioclase websterite vein.

al Session
Cs^+ beam[c]
n.a.
C2
C2
C1, C2
C2
n.a.
C2
C2
C2
C2
C2
C2

untA was
ing the Cs+

olivine

This is a preprint, the final version is subject to change, of the American Mineralogist (MSA)
Cite as Authors (Year) Title. American Mineralogist, in press.
DOI: https://doi.org/10.2138/am-2019-6516

Table 2. Average major element composition of sulfide grains in wt% by sulfide category.*

Sample	Sulfide	Fe	Co	Ni	Cu	S	Zn	Si	O	Sum	n	Session	Phase
Pentlandite (Pn) sulfides													
HLY0102-70-75	Sulf10	31.72	0.28	33.05	0.24	31.83	0.03	0.01	0.39	97.56	7	2016	Pn
PS59-235-01	Sulf1B	41.76	0.25	23.46	0.13	30.99	0.03	0.02	0.09	96.74	3	2014	Pn
PS59-235-01	Sulf2A	42.92	0.30	24.16	b.d.	31.66	0.02	b.d.	b.d.	99.05	3	2014	Pn
PS59-235-01	Sulf3	37.14	0.26	30.06	b.d.	32.09	0.01	b.d.	b.d.	99.55	8	2014	Pn
PS59-235-01	Sulf7A	36.62	0.59	28.80	b.d.	31.25	b.d.	0.21	b.d.	97.47	3	2014	Pn
PS59-235-01	Sulf7B	42.23	0.37	23.79	0.92	31.98	0.01	0.01	b.d.	99.30	6	2014	Pn
PS59-235-01	Sulf7C	43.86	0.25	22.01	b.d.	32.32	0.02	0.01	b.d.	98.47	5	2014	Pn
PS59-235-01	Sulf9A	34.74	0.24	32.77	b.d.	31.21	b.d.	b.d.	b.d.	98.96	2	2014	Pn
PS59-235-01	Sulf9B	32.65	0.21	33.01	2.53	31.47	0.00	b.d.	b.d.	99.86	2	2014	Pn
PS59-235-01	Sulf9C	34.18	0.25	31.69	0.36	30.98	0.01	0.05	b.d.	97.52	3	2014	Pn
PS59-235-01	Sulf9D	31.34	0.27	34.06	0.69	31.30	b.d.	0.01	b.d.	97.66	2	2014	Pn
PS59-235-01	Sulf11A	46.60	0.27	18.38	b.d.	32.65	0.05	b.d.	0.54	98.49	7	2016	Pn
PS59-235-01	Sulf11B	42.08	0.29	22.07	1.08	31.82	0.04	0.01	0.56	97.94	8	2016	Pn
PS59-235-17	Sulf1	37.86	0.27	27.29	b.d.	32.97	0.05	0.01	0.35	98.79	5	2016	Pn
PS59-235-17	Sulf2A	45.46	0.28	20.23	b.d.	33.37	0.07	0.00	0.46	99.86	4	2016	Pn
PS59-235-17	Sulf4	42.48	0.34	23.13	b.d.	33.51	0.04	0.00	0.38	99.88	5	2016	Pn
PS59-235-17	Sulf5A	43.49	0.13	22.05	b.d.	34.99	0.02	0.01	0.45	101.12	5	2016	Pn
PS59-235-17	Sulf5B	41.88	0.24	23.29	0.03	34.76	0.04	0.01	0.39	100.65	5	2016	Pn
PS59-235-18	Sulf3A	41.07	0.13	24.98	0.14	31.89	0.03	b.d.	0.61	98.85	6	2016	Pn
PS59-235-18	Sulf3B	43.64	0.29	21.10	b.d.	32.81	0.05	0.01	0.78	98.68	7	2016	Pn
PS59-235-18	Sulf7	43.65	0.34	22.53	0.16	32.41	0.04	0.00	0.47	99.61	6	2016	Pn
PS59-235-18	Sulf10A	40.67	0.20	25.11	b.d.	31.64	0.02	0.01	0.71	98.36	6	2016	Pn
PS59-235-18	Sulf10B	40.38	0.36	25.39	b.d.	32.13	0.03	0.01	0.45	98.75	6	2016	Pn
PS59-235-18	Sulf10C	41.32	0.24	24.32	0.19	32.47	0.03	0.01	0.50	99.07	6	2016	Pn
PS59-235-18	Sulf10D	40.38	0.21	24.14	0.97	31.91	0.05	0.01	0.54	98.21	5	2016	Pn
PS59-238-75	Sulf20A	32.09	0.35	33.11	b.d.	31.68	0.05	0.02	0.34	97.64	6	2016	Pn
PS59-238-75	Sulf20C	35.01	0.23	30.22	b.d.	31.87	0.02	0.03	0.41	97.79	7	2016	Pn
PS59-238-75	Sulf20D	32.15	0.26	32.97	b.d.	31.70	0.03	0.01	0.33	97.45	5	2016	Pn
Van7-85-49	Sulf8A	36.14	0.31	24.17	3.89	35.27	0.04	0.02	0.54	100.37	7	2016	Pn
Van7-85-49	Sulf8B	35.33	0.42	24.36	3.52	35.23	0.04	0.03	0.51	99.44	7	2016	Pn
Van7-96-21M	Sulf4A	35.56	0.35	29.93	0.80	32.66	0.01	0.02	0.37	99.70	1	2016	Pn
Cu-bearing sulfides: Intergrowths of pentlandite and chalcopyrite (Cp)													
PS59-235-18	Sulf5Pn	35.73	0.27	29.33	1.26	31.28	0.03	0.02	0.59	98.51	7	2016	Pn
PS59-235-18	Sulf8Ccp	30.98	0.02	0.80	32.15	32.72	0.04	0.01	0.79	97.50	7	2016	Ccp
PS59-235-18	Sulf8Pn	42.89	0.51	22.44	0.22	32.21	0.02	0.00	0.43	98.73	6	2016	Pn
Van7-96-21V	Sulf1Ccp	29.52	b.d.	0.27	33.87	32.37	0.05	0.02	0.83	96.94	5	2016	Ccp
Van7-96-21V	Sulf1Pn	27.83	0.76	37.85	b.d.	31.62	0.04	0.01	0.43	98.52	5	2016	Pn
Van7-96-21V	Sulf3Ccp	30.60	b.d.	3.49	29.31	33.34	b.d.	0.14	0.86	97.74	6	2016	Ccp
Van7-96-21V	Sulf3Pn	35.89	0.37	29.66	b.d.	32.42	0.02	0.02	0.37	98.74	3	2016	Pn
Cu-bearing sulfides: Fine-scale (<1 um) intergrowths of pentlandite and chalcopyrite													
PS59-235-01	Sulf1A	40.89	0.25	20.88	1.98	32.47	0.02	0.03	0.47	97.00	3	2014	Pn+Ccp
PS59-235-01	Sulf8	43.70	0.32	21.93	2.17	32.40	b.d.	0.01	b.d.	100.54	14	2014	Pn+Ccp
PS59-235-01	Sulf20	42.60	0.24	19.95	2.66	32.67	0.01	0.02	0.56	98.72	10	2016	Pn+Ccp
PS59-235-17	Sulf2B	40.78	0.32	21.69	5.34	34.37	0.05	0.07	0.78	103.39	4	2016	Pn+Ccp
PS59-235-17	Sulf2C	42.69	0.14	22.58	0.19	34.51	0.07	0.04	0.53	100.75	4	2016	Pn+Ccp
Van7-85-47	Sulf5	37.44	0.72	25.10	1.31	35.06	0.11	0.02	0.73	100.48	7	2016	Pn+Ccp
Van7-85-49	Sulf7B	37.41	0.21	5.85	19.82	35.91	0.04	0.01	0.60	99.86	8	2016	Pn+Ccp
Van7-85-49	Sulf10A	36.83	0.27	20.26	8.37	33.49	0.05	0.01	0.37	99.66	5	2016	Pn+Ccp
Van7-96-21M	Sulf4B	34.64	0.30	26.85	4.60	32.46	0.02	0.07	0.48	99.42	6	2016	Pn+Ccp
Van7-96-28	Sulf7	32.56	0.33	19.14	12.84	33.08	0.03	0.01	0.67	98.68	4	2016	Pn+Ccp

Van7-96-28	Sulf9	34.73	0.32	24.91	4.87	33.58	b.d.	0.01	0.55	98.97	5	2016	Pn+Ccp
Van7-96-28	Sulf10A	32.94	0.29	25.70	6.58	33.67	b.d.	0.02	0.55	99.76	9	2016	Pn+Ccp
Van7-96-28	Sulf11	30.83	0.33	19.89	12.45	33.95	0.05	0.02	0.38	97.89	5	2016	Pn+Ccp
Van7-96-28	Sulf12A	32.08	0.30	19.63	12.24	33.24	0.03	0.01	0.39	97.92	4	2016	Pn+Ccp
Van7-96-28	Sulf14	34.60	0.29	26.50	3.65	32.91	0.02	0.03	0.53	98.53	5	2016	Pn+Ccp
Van7-96-28	Sulf15	34.48	0.19	20.49	10.04	32.69	0.04	0.01	0.37	98.31	5	2016	Pn+Ccp
Van7-96-28	Sulf16A	28.66	0.21	19.94	15.27	34.20	0.05	0.00	0.36	98.70	4	2016	Pn+Ccp
Van7-96-28	Sulf16B	32.45	0.35	24.62	7.04	33.64	0.07	0.02	0.39	98.56	4	2016	Pn+Ccp
Altered sulfides: Grains that are entirely altered (based on petrographic observations)													
PS59-235-01	Sulf1C-alt	34.70	0.27	22.96	1.12	22.27	0.02	0.58	6.79	88.71	3	2014	Pn+Ccp
PS59-235-01	Sulf1D-alt	40.52	0.21	22.45	0.13	20.97	b.d.	0.66	12.16	97.09	2	2014	Pn
PS59-235-01	Sulf10A-alt	24.48	0.37	26.02	2.34	18.58	1.86	2.53	17.15	93.33	1	2014	Pn+Ccp
PS59-235-18	Sulf2A-alt	42.77	0.50	23.03	b.d.	31.56	0.03	0.03	1.42	99.34	10	2016	Pn
PS59-235-18	Sulf2B-alt	42.61	0.21	21.37	0.21	30.93	0.04	0.15	2.80	98.33	8	2016	Pn
PS59-238-75	Sulf20B-alt	25.69	0.30	31.10	0.03	26.01	0.02	2.47	9.02	94.64	7	2016	Pn
Van7-85-47	Sulf2-alt	26.83	0.81	23.22	2.18	28.22	0.07	2.64	12.31	96.27	3	2016	Pn+Ccp
Van7-85-49	Sulf7A-alt	21.81	0.51	30.03	2.54	23.47	0.04	1.50	19.18	99.06	2	2016	Pn+Ccp
Van7-85-49	Sulf10A-alt	29.10	0.26	21.77	2.15	30.71	0.05	1.16	12.31	97.52	3	2016	Pn+Ccp
Van7-85-49	Sulf10B-alt	24.04	0.93	27.91	0.84	20.35	0.08	1.18	17.88	93.21	3	2016	Pn
Van7-85-49	Sulf10C-alt	19.34	0.54	30.12	0.82	20.09	0.04	1.32	17.69	89.96	3	2016	Pn
Van7-85-49	Sulf11-alt	26.04	1.06	23.91	1.76	34.25	0.00	0.98	8.69	96.69	3	2016	Pn+Ccp
Van7-85-49	Sulf11-mag	69.82	b.d.	0.30	0.12	0.10	0.03	0.12	26.49	96.97	3	2016	Magnetite
Van7-85-49	Sulf13C-alt	12.16	1.83	28.94	10.44	28.60	0.02	1.58	12.14	95.70	5	2016	Pn+Ccp
Van7-96-21M	Sulf3B-alt	28.77	0.71	29.10	1.85	29.23	0.04	1.82	5.32	96.83	3	2016	Pn+Ccp
Van7-96-21M	Sulf3C-alt	21.80	0.43	33.53	2.33	29.58	0.02	2.14	8.08	97.90	3	2016	Pn+Ccp
Van7-96-21M	Sulf4C-alt	34.13	0.49	27.72	1.20	31.08	0.07	0.32	1.69	96.68	2	2016	Pn+Ccp
Van7-96-21V	Sulf2-alt	36.47	0.43	26.66	0.40	31.98	0.03	0.25	2.80	99.03	2	2016	Pn
Van7-96-28	Sulf8-alt	32.74	0.30	26.90	3.87	32.89	0.03	1.05	4.16	101.94	3	2016	Pn+Ccp
Van7-96-28	Sulf12B-alt	25.53	0.41	27.66	5.79	33.45	0.04	0.58	3.45	96.91	3	2016	Pn+Ccp
Van7-96-28	Sulf13B-alt	35.30	0.31	25.42	1.45	32.44	0.04	0.50	2.42	97.89	5	2016	Pn+Ccp
Altered sulfides: Altered parts of grains (identified based on >1 wt% oxygen)													
PS59-235-01	Sulf1A-alt	35.24	0.23	18.86	1.82	29.05	b.d.	2.04	8.11	95.35	2	2014	Pn+Ccp
PS59-235-01	Sulf1B-alt	38.82	0.26	24.25	b.d.	28.31	0.01	0.30	4.96	96.90	6	2014	Pn
PS59-235-01	Sulf11B-alt	40.06	0.30	22.10	2.03	30.39	b.d.	0.44	3.57	98.89	1	2016	Pn
PS59-235-01	Sulf11A-alt	41.82	0.24	22.29	0.60	31.06	0.06	b.d.	1.48	97.55	2	2016	Pn
PS59-235-01	Sulf20-alt	30.55	0.21	16.27	8.43	25.82	0.03	0.17	3.66	85.13	8	2016	Pn+Ccp
PS59-235-18	Sulf5Ccp-alt	20.22	0.20	14.32	24.58	27.45	0.04	0.54	8.40	95.76	6	2016	Ccp
PS59-235-18	Sulf8Ccp-alt	30.92	b.d.	1.16	31.77	32.28	0.03	0.04	1.73	97.93	2	2016	Ccp
Van7-85-47	Sulf5-alt	33.41	0.78	25.24	3.69	34.20	0.04	0.23	2.23	99.84	3	2016	Pn+Ccp
Van7-85-49	Sulf7B-alt	32.57	0.25	10.17	15.45	29.45	b.d.	2.06	9.87	99.81	2	2016	Pn+Ccp
Van7-85-49	Sulf8A-alt	39.16	0.22	20.53	1.58	36.59	0.03	0.11	1.42	99.63	3	2016	Pn
Van7-85-49	Sulf8B-alt	31.34	1.31	29.39	0.14	35.58	0.03	0.06	1.51	99.36	3	2016	Pn
Van7-96-21V	Sulf1Ccp-alt	27.23	b.d.	0.18	33.62	24.57	0.07	0.07	2.80	88.55	6	2016	Ccp
Van7-96-21V	Sulf3Ccp-alt	30.82	0.16	27.51	6.38	31.93	0.01	0.37	2.51	99.67	3	2016	Ccp
Van7-96-28	Sulf10A-alt	34.18	0.28	17.49	4.65	25.14	0.05	3.36	12.96	98.11	5	2016	Pn+Ccp

*Standard deviations of the averages reported in this table are provided in supplemental Table S2; b.d. indicates below detection.

This is a preprint, the final version is subject to change, of the American Mineralogist (MSA)
Cite as Authors (Year) Title. American Mineralogist, in press.
DOI: https://doi.org/10.2138/am-2019-6516

Table 3. Trace element concentrations (ppm) and ratios of unaltered sulfides, averaged by grain[a].

Sample	Sulfide	Phase	Number of O_2^- analyses	Pb (ppm)	1σ	Fe/Ni	1σ	Number of Cs^+ analyses	As (ppm)	1σ	Se (ppm)
Pentlandite (Pn) sulfides											
HLY0102-70-75	Sulf10	Pn	5	5.88	1.92	0.98	0.02	1	9	2	93
PS59-201-39	Sulf1	Pn	3	2.69	0.59	1.28	0.01	1	7	2	141
PS59-201-39	Sulf2A[b]	Pn	3	3.06	0.53	1.66	0.02	2	< 1.5		150
PS59-201-39	Sulf4A	Pn	2	2.85	0.10	1.74	0.04	2	8	5	116
PS59-201-39	Sulf4B	Pn	2	4.61	0.46	1.74	0.26	1	7	2	122
PS59-235-01	Sulf1B	Pn	9	2.51	0.16	1.58	0.36	2	< 11		222
PS59-235-01	Sulf2A	Pn	1	3.12	3.11	1.83	0.04	2	< 5		129
PS59-235-01	Sulf3	Pn	5	2.33	0.10	1.19	0.04	3	b.d.		95
PS59-235-01	Sulf4	Pn						2	31	22	98
PS59-235-01	Sulf6	Pn						1	< 5		231
PS59-235-01	Sulf7A	Pn	1	2.94	2.98	1.36	0.03	1	6	2	184
PS59-235-01	Sulf7B	Pn	3	3.14	0.44	1.65	0.07	3	< 5		106
PS59-235-01	Sulf7C	Pn	2	2.89	0.87	1.94	0.07	2	b.d.		82
PS59-235-01	Sulf8Pn	Pn	10	5.72	0.85	1.86	0.12	6	< 12		100
PS59-235-01	Sulf9A	Pn	1	2.78	2.86	1.09	0.02	1	b.d.		91
PS59-235-01	Sulf9B	Pn	1	2.37	2.53	1.08	0.02				
PS59-235-01	Sulf9C	Pn	1	2.26	2.44	1.70	0.04				
PS59-235-01	Sulf9D	Pn	1	3.19	3.15	1.03	0.02				
PS59-235-01	Sulf11A	Pn	3	2.33	0.22	1.87	0.09				
PS59-235-01	Sulf11B	Pn	3	2.29	0.14	1.98	0.03				
PS59-235-01	Sulf12A	Pn	1	2.71	2.01	1.55	0.09				
PS59-235-01	Sulf12B	Pn	1	3.41	2.34	2.33	0.13				
PS59-235-01	Sulf14A	Pn	1	2.08	1.65	1.49	0.09				
PS59-235-01	Sulf14B	Pn	2	3.29	0.65	1.91	0.02				
PS59-235-01	Sulf15A	Pn	1	2.27	1.76	1.85	0.11				
PS59-235-01	Sulf15B	Pn	1	2.04	1.63	1.68	0.10				
PS59-235-01	Sulf16	Pn	1	2.03	1.62	1.43	0.08				
PS59-235-01	Sulf17A	Pn	1	2.79	2.05	1.57	0.09				
PS59-235-01	Sulf17B	Pn	1	3.49	2.37	1.47	0.08				
PS59-235-01	Sulf17C	Pn	1	2.58	1.94	1.39	0.08				
PS59-235-01	Sulf18	Pn	1	5.26	2.94	1.34	0.08				
PS59-235-01	Sulf19	Pn	2	2.97	0.02	1.85	0.01				
PS59-235-17	Sulf1	Pn	6	2.64	0.15	1.42	0.05	3	17	23	122
PS59-235-17	Sulf2A	Pn	8	2.70	0.45	2.15	0.08	3	102	89	58
PS59-235-17	Sulf3	Pn	4	2.73	0.21	1.73	0.06	1	23	4	67
PS59-235-17	Sulf4	Pn	9	2.47	0.10	1.73	0.02	3	15	12	154
PS59-235-17	Sulf5A	Pn	4	2.47	0.16	1.87	0.06	1	< 1.5		97
PS59-235-17	Sulf5B	Pn	2	2.88	0.14	1.71	0.00	1	46	7	107
PS59-235-17	Sulf6	Pn	4	2.58	0.04	1.16	0.01	1	< 1.5		93
PS59-235-18	Sulf1A	Pn	2	2.37	0.12	2.17	0.00				
PS59-235-18	Sulf1B	Pn	2	2.34	0.32	2.03	0.07				
PS59-235-18	Sulf3A	Pn	1	2.63	1.96	1.60	0.09				
PS59-235-18	Sulf3B	Pn	2	2.18	0.11	2.00	0.07				
PS59-235-18	Sulf4	Pn	1	2.51	1.90	1.12	0.07				
PS59-235-18	Sulf6	Pn	1	2.29	1.78	1.58	0.09				

This is a preprint, the final version is subject to change, of the American Mineralogist (MSA)
Cite as Authors (Year) Title. American Mineralogist, in press.
DOI: https://doi.org/10.2138/am-2019-6516

PS59-235-18	Sulf7	Pn	6	2.91	0.58	1.85	0.05				
PS59-235-18	Sulf8B	Pn	2	2.99	0.68	1.55	0.04				
PS59-235-18	Sulf8C	Pn	1	2.51	1.90	1.10	0.06				
PS59-235-18	Sulf9	Pn	1	2.43	1.86	1.57	0.09				
PS59-235-18	Sulf10A	Pn	3	3.52	0.35	1.75	0.25				
PS59-235-18	Sulf10B	Pn	2	2.71	0.66	1.60	0.02				
PS59-235-18	Sulf10C	Pn	5	2.50	0.35	1.45	0.12				
PS59-235-18	Sulf10D	Pn	1	2.45	1.87	1.64	0.10				
PS59-238-75	Sulf11A	Pn	4	2.39	0.22	1.02	0.10	5	5	2	79
PS59-238-75	Sulf11B	Pn	3	3.73	0.14	1.19	0.02				
PS59-238-75	Sulf11C	Pn	1	2.22	1.74	1.27	0.07				
PS59-238-75	Sulf11D	Pn	1	2.50	1.90	1.27	0.07				
PS59-238-75	Sulf12B	Pn	1	2.80	2.05	1.61	0.09				
PS59-238-75	Sulf12C	Pn	1	2.95	2.13	1.41	0.08				
PS59-238-75	Sulf13A	Pn	1	2.40	1.84	1.32	0.08				
PS59-238-75	Sulf13B	Pn	1	4.22	2.65	1.34	0.08				
PS59-238-75	Sulf14A	Pn	6	2.56	0.33	1.44	0.07	11	35	53	86
PS59-238-75	Sulf14B	Pn	2	2.71	0.18	1.14	0.01	1	5	2	125
PS59-238-75	Sulf15A	Pn	3	3.55	1.44	1.07	0.03	1	15	3	49
PS59-238-75	Sulf15B	Pn	3	3.87	0.83	1.11	0.06	2	< 10		72
PS59-238-75	Sulf16A	Pn	1	3.80	2.50	0.96	0.06	1	4	2	45
PS59-238-75	Sulf16B	Pn	2	3.92	0.03	1.11	0.04	2	28	33	88
PS59-238-75	Sulf16C	Pn	2	3.01	0.49	1.07	0.00				
PS59-238-75	Sulf17	Pn	1	4.59	2.76	1.20	0.07				
PS59-238-75	Sulf18	Pn	1	2.79	2.05	1.08	0.06				
PS59-238-75	Sulf19	Pn	2	3.15	0.27	1.09	0.01	1	7	2	106
PS59-238-75	Sulf20A	Pn	1	3.63	2.43	1.07	0.06				
PS59-238-75	Sulf20C	Pn	1	3.64	2.43	1.47	0.09				
Van7-85-47	Sulf1	Pn	1	2.73	2.04	1.60	0.09	1	4	2	120
Van7-85-47	Sulf3	Pn	3	2.56	0.08	1.39	0.14				
Van7-85-47	Sulf4A	Pn	5	2.59	0.45	1.43	0.05	2	< 32		123
Van7-85-49	Sulf6	Pn	5	3.42	0.83	1.08	0.19	3	274	199	126
Van7-85-49	Sulf8A	Pn	6	2.51	0.07	1.51	0.13	4	113	153	155
Van7-85-49	Sulf8B	Pn	8	2.98	0.52	1.41	0.19	3	196	176	96
Van7-85-49	Sulf9A	Pn	2	2.56	0.23	1.49	0.16	1	122	19	146
Van7-85-49	Sulf9B	Pn	1	2.45	1.89	1.81	0.10				
Van7-85-49	Sulf12	Pn	3	2.42	0.03	0.88	0.08	3	72	107	201
Van7-96-21M	Sulf2A	Pn	3	2.60	0.14	1.10	0.08	3	7	4	95
Van7-96-21M	Sulf4A	Pn	1	2.82	2.09	1.25	1.25	2	69	91	102
Cu-bearing sulfides: Intergrowths of pentlandite and chalcopyrite (Ccp)											
PS59-235-18	Sulf5Ccp	Ccp	1	2.94	2.12	3.44	0.20				
PS59-235-18	Sulf5Pn	Pn	2	2.39	0.47	1.18	0.03				
PS59-235-18	Sulf8ACcp	Ccp	1	2.22	1.74	2.83	0.16				
PS59-235-18	Sulf8APn	Pn	2	2.28	0.07	1.81	0.12				
Van7-96-21V	Sulf1Ccp	Ccp	1	3.75	2.49	145.41	8.46	1	32	5	75
Van7-96-21V	Sulf1Pn	Pn	3	4.46	1.10	1.33	0.35	2	9	4	113
Van7-96-21V	Sulf3Ccp	Ccp	1	5.36	2.96	12.23	0.71	1	56	9	150
Van7-96-21V	Sulf3Pn	Pn	1	3.25	2.29	1.56	0.09				
Cu-bearing sulfides: Fine-scale (<1 um) intergrowths of pentlandite and chalcopyrite											
PS59-235-01	Sulf1A	Pn+Ccp	4	8.31	2.54	1.78	0.10				

This is a preprint, the final version is subject to change, of the American Mineralogist (MSA)
Cite as Authors (Year) Title. American Mineralogist, in press.
DOI: https://doi.org/10.2138/am-2019-6516

PS59-235-01	Sulf8	Pn+Ccp	3	15.40[c]	11.22	1.95	0.09				
PS59-235-01	Sulf20	Pn+Ccp	4	8.70	2.51	1.74	0.09				
PS59-235-17	Sulf2B	Pn+Ccp	2	2.46	0.04	2.07	0.09	2	250	265	82
PS59-235-17	Sulf2C	Pn+Ccp	2	3.64	0.54	1.89	0.00	1	32	5	82
Van7-85-47	Sulf5	Pn+Ccp	2	2.47	0.17	1.43	0.16	1	850	130	108
Van7-85-49	Sulf7B	Pn+Ccp	1	2.41	1.87	3.93	0.23				
Van7-85-49	Sulf10A	Pn+Ccp	4	2.41	0.02	1.99	0.52	3	272	380	127
Van7-85-49	Sulf13A	Pn+Ccp	2	3.48	0.57	1.48	0.08	1			127
Van7-85-49	Sulf13B	Pn+Ccp	2	3.21	2.26	4.00	0.03				
Van7-96-21M	Sulf1	Pn+Ccp	5	3.35	1.12	1.14	0.05	4	229	306	109
Van7-96-21M	Sulf4B	Pn+Ccp	2	11.74[c]	9.38	1.24	0.07	1	83	13	138
Van7-96-28	Sulf7	Pn+Ccp	2	4.42	1.19	1.86	0.08	3	16	10	196
Van7-96-28	Sulf9	Pn+Ccp	3	4.09	0.90	1.33	0.03	2	105	145	79
Van7-96-28	Sulf10A	Pn+Ccp	6	12.10[c]	4.75	1.34	0.31	2	1088	1185	231
Van7-96-28	Sulf11	Pn+Ccp	2	6.15	1.58	1.57	0.07	2	199	64	110
Van7-96-28	Sulf12A	Pn+Ccp	5	32.30[c]	42.49	1.72	0.29	2	228	303	212
Van7-96-28	Sulf12B	Pn+Ccp	2	36.19[c]	0.68	1.35	0.25				
Van7-96-28	Sulf14	Pn+Ccp	5	6.65	0.93	1.42	0.04	2	95	129	173
Van7-96-28	Sulf15	Pn+Ccp	6	10.59[c]	5.14	1.49	0.18				
Van7-96-28	Sulf16A	Pn+Ccp	2	7.43	1.37	1.38	0.07				
Van7-96-28	Sulf16B	Pn+Ccp	1	4.84	2.84	1.40	0.08				
Van7-96-28	Sulf17	Pn+Ccp	3	5.61	1.10	1.61	0.05	2	73	94	98

[a]For each element, 1σ is the standard deviation of the averaged analyses. If only one measurement was made, then the val
with multiple analyses, the elements Pb, Se, and Au are homogeneous (except where indicated for Pb), whereas the other
[b]Sulfide is surrounded by carbonate.

[c]Sulfide has heterogeneous Pb abundances, based on multiple analyses that are not within error of each other.

This is a preprint, the final version is subject to change, of the American Mineralogist (MSA)
Cite as Authors (Year) Title. American Mineralogist, in press.
DOI: https://doi.org/10.2138/am-2019-6516

1σ	Sb (ppm)	1σ	Te (ppm)	1σ	Ag (ppm)	1σ	Au (ppm)	1σ	Cl (ppm)	1σ	Cu/S_2	1σ
8	83	4	5	3	42	9			218.1	0.2	0.696	0.004
13	18	4	< 4		26	5			104.6	0.5	0.086	0.001
28	26	7	19	6	4	2	0.0354	0.0169	4	3	0.016	0.002
5	45	34	< 4		35.4	0.4			47	12	0.175	0.016
11	57	5	28	2	23	5			49.3	0.3	0.120	0.001
35	52	44	220	199					22	29	0.012	0.013
27	10	10							11	14	0.434	0.586
16	4	2	87	93					3	4	0.040	0.066
13	37	32	15	7					42	42	0.102	0.146
44	7	4	29	6					85	1	0.944	0.012
35	14	6	104	21					52.0	0.5	0.025	0.001
19	12	9	7	3					48	28	0.035	0.020
20	10	2	12	5					18	9	0.020	0.011
12	52	106	< 11						27	29	0.062	0.060
17	9	5	< 4						1.33	0.02	0.010	0.001
18	25	22	6	4	15	12	0.0187	0.0147	14	8	0.128	0.065
6	38	38	<4		41	19	0.0113	0.0106	251	138	0.305	0.216
5	52	5	7	3	60	13	0.0061	0.0029	238	1	0.175	0.001
38	57	58	41	62	42	5	0.0150	0.0082	36	11	0.729	0.152
8	20	4	5	3	38	8	0.0054	0.0026	17.2	0.1	0.512	0.004
9	49	5	18	2	44	9	0.0171	0.0082	28.0	0.2	1.159	0.008
8	18	4	<4		23	5	0.0044	0.0021	9.26	0.06	0.149	0.001

15	29	16	23	13	26	22			25	24	0.031	0.014
16	23	10	< 21		26	21			31	33	0.284	0.286
11	45	5	18	2	33	7			48.1	0.3	0.155	0.001
4	11	3	< 4		10	2			6.99	0.06	0.192	0.002
10	46	38	< 4		58	49			91	111	0.423	0.147
3	32	5	< 4		54	12			215.6	0.8	0.463	0.002
5	41	8	< 4		56	2			23	17	0.315	0.284
9	28	4	10	2	24	5			20.6	0.1	0.194	0.001
10	23	4	< 4		15	3			8.06	0.06	0.197	0.001
8	15	7	< 4		15	6			239	60	0.126	0.087
45	314	20	22	17	295	36			52	3	0.141	0.080
19	64	29	34	17	54	30			84	76	0.331	0.150
33	66	50	< 4		113	117			277	155	0.399	0.268
13	68	4	13	2	78	17			43.0	0.3	0.211	0.002
70	105	50	57	37	81	13			420	198	0.788	0.082
14	27	10	5	1	22	14	0.0081	0.0016	78	91	0.521	0.683
27	54	4	5	1	49	13	0.0357	0.0100	41	3	1.358	0.512
6	55	5	< 4		9	2	0.0873	0.0417	1.54	0.02	7.925	0.049
21	122	19	< 5		65	28	0.0457	0.0112	51	4	1.070	0.113
14	146	2	6	3	109	25	0.0206	0.0099	23.2	0.2	2.001	0.012

This is a preprint, the final version is subject to change, of the American Mineralogist (MSA)
Cite as Authors (Year) Title. American Mineralogist, in press.
DOI: https://doi.org/10.2138/am-2019-6516

26	36	3	9	8	45	45	0.0198	0.0186	148	131	0.976	1.296
7	34	5	4	3	40	8	0.0309	0.0148	143.5	1.4	0.499	0.006
9	64	4	8	3	78	17			1.5	0.02	0.442	0.002
62	98	95	22	12	65	56			93	48	0.964	0.751
11	122	2	7	3	159	38			250.7	1.7	2.114	0.012
28	86	82	< 7		70	41	0.0079	0.0029	94	63	1.281	1.018
12	91	3	< 4		138	32	0.0848	0.0406	106	1	1.743	0.011
7	79	43	26	23	111	39	0.0134	0.0012	143	141	3.020	0.469
22	40	19	< 4		49	19	0.0025	0.0012	723	417	1.643	0.604
13	186	98	9	7	139	53	0.0121	0.0031	360	49	5.930	2.669
31	39.0	0.2	5	1	62	33	0.0059	0.0049	159	72	1.464	0.211
51	135	71	8	4	165	40	0.0104	0.0076	207	62	8.552	5.694
76	219	282	30	29	95	77	0.3905	0.5363	75	89	3.369	3.930
6	197	2	16	12	118	18	0.0073	0.0002	236	40	6.898	0.322

ue corresponds to the 1σ analytical error, which is based on reproducibility of the standards. For grains
trace elements are heterogeneous.

This is a preprint, the final version is subject to change, of the American Mineralogist (MSA)
Cite as Authors (Year) Title. American Mineralogist, in press.
DOI: https://doi.org/10.2138/am-2019-6516

Table 4. Trace element concentrations (ppm) and ratios in altered sulfides, averaged by grain[a].

Sample	Sulfide	Number of O_2^- analyses	Pb (ppm)	1σ	Fe/Ni	1σ	Number of Cs^+ analyses	As (ppm)	1σ	Se (ppm)	1σ	Sb (ppm)
Altered sulfides: Altered parts of grains												
HLY0102-70-62	Sulf4	2	6.8	2.2	1.32	0.06						
HLY0102-70-62	Sulf6	2	4.5	0.01	0.93	0.01						
HLY0102-70-75	Sulf7A	9	4.7	1.6	1.04	0.06	4	565	910	181	51	76
PS59-201-39	Sulf3	2	11.2	3.7	1.62	0.03						
PS59-235-01	Sulf1E	3	4.6	3.2	2.43	0.67	1	109	22	501	95	932
PS59-235-01	Sulf10A	3	44.4	27.3	0.82	0.08						
PS59-235-01	Sulf17D	1	7.0	3.2	0.92	0.05						
PS59-235-01	Sulf17E	1	6.7	3.2	0.85	0.05						
Van7-85-47	Sulf2	2	3.2	0.3	0.86	0.07	2	135	12	97	33	213
Van7-85-49	Sulf7A	15	3.1	0.9	0.65	0.12	3	1906	1693	174	26	447
Van7-85-49	Sulf10A	3	2.5	0.2	1.54	0.39	3	272	380	127	62	98
Van7-85-49	Sulf10B	11	3.1	0.8	0.52	0.07	4	1730	1499	59	10	410
Van7-85-49	Sulf10C	4	3.1	0.8	0.43	0.03	2	938	1136	57	14	695
Van7-85-49	Sulf11	3	2.7	0.3	1.00	0.05	1	224	34	277	30	303
Van7-96-21M	Sulf2B						1	12	2	108	9	129
Van7-96-21V	Sulf2	3	5.2	3.0	2.03	0.84	1	9	2	149	14	78
Van7-96-28	Sulf13B	1	5.3	2.9	1.88	0.11	1	18	3	161	15	126
Altered sulfides: Grains that are entirely altered												
HLY0102-70-62	Sulf1	1	3.4	2.4	1.18	0.07						
HLY0102-70-62	Sulf2	2	6.3	1.8	1.22	0.14						
HLY0102-70-62	Sulf5D	1	14.5	2.9	1.34	0.08						
HLY0102-70-75	Sulf7B	1	7.9	3.3	0.98	0.06						
HLY0102-70-75	Sulf9	1	7.6	3.3	0.88	0.05						
PS59-201-39	Sulf2B	2	5.7	4.0	1.40	0.08	1	4	2	163	15	30
PS59-235-01	Sulf1C	2	22.9	12.1	1.31	0.06	1	68	14	202	38	84
PS59-235-01	Sulf1D	2	10.7	2.3	1.05	0.06	1	32	7	169	32	165
PS59-235-18	Sulf2A	2	2.5	0.2	2.03	0.28						
PS59-235-18	Sulf2B	1	2.6	1.9	2.31	0.13						
PS59-238-75	Sulf20B	1	4.1	2.6	0.92	0.05						
Van7-85-49	Sulf13C	1	3.4	2.4	0.60	0.03						
Van7-96-21M	Sulf4C	1	2.9	2.1	1.38	0.08	1	39	6	156	14	81
Altered sulfides: Grains with abundant cracks												
HLY0102-70-62	Sulf3A	2	3.9	0.9	1.21	0.13						
HLY0102-70-62	Sulf3B	3	4.3	2.2	1.20	0.04						
HLY0102-70-62	Sulf5B	2	18.0	14.8	1.44	0.07						
HLY0102-70-62	Sulf7A	9	4.7	1.6	1.04	0.06						
PS59-201-39	Sulf6	2	6.9	2.0	1.35	0.01	1	21	3	111	9	21
Van7-85-47	Sulf4B	3	2.8	0.2	1.31	0.12	1	7	2	144	13	35
Van7-96-21M	Sulf3B	3	8.2	7.1	1.23	0.08	1	87	13	100	8	129
Van7-96-21M	Sulf3C	1	8.1	3.3	1.08	0.06						
Van7-96-21M	Sulf5	1	6.3	3.1	1.56	0.09						
Van7-96-28	Sulf8	2	8.3	1.5	1.27	0.03	1	237	36	208	21	98
Van7-96-28	Sulf10B	1	15.7	2.7	1.12	0.06	2	144	19	109	12	368
Van7-96-28	Sulf10C	3	48.6	16.4	1.25	0.23						
Van7-96-28	Sulf12B	2	36.2	19.8	1.35	0.25						
Van7-96-28	Sulf13A	1	31.1	1.3	1.12	0.06						

[a]For each element, 1σ is the standard deviation of the averaged analyses. If only one measurement was made, then the value c
Se, and Au are homogeneous, whereas the other trace elements are heterogeneous.

This is a preprint, the final version is subject to change, of the American Mineralogist (MSA)
Cite as Authors (Year) Title. American Mineralogist, in press.
DOI: https://doi.org/10.2138/am-2019-6516

1σ	Te (ppm)	1σ	Ag (ppm)	1σ	Au (ppm)	1σ	Cl (ppm)	1σ	Cu/S_2	1σ
38	36	12	85	54			69.37	85.62	0.03	0.02
62	160	32					12006	229		
157	11	2	149	2			36.64	4.26	0.3	0.2
62	29	17	383	94			40.4	26.4	0.9	0.4
95	22	12	65	56			92.5	48.2	1.0	0.8
87	11	2	188	35			179.6	137.2	0.12	0.03
73	9	1	205	32			723	417	0.13	0.02
1	38	3	291	79			395	3	0.551	0.003
2	5	3	60	13	0.012	0.006	105.0	0.6	2.20	0.01
4	5	3	49	10	0.094	0.045	53.8	0.3	1.357	0.009
2	51	4	72	16			92.7	0.6	0.185	0.002
5	22	2	9	2			86.5	0.7	0.0267	0.0006
9	41	8					212	3		
12	72	14					78.8	0.9		
4	< 4		60	13	0.202	0.097	132.3	0.8	2.43	0.01
4	8	3	28	6			62.5	0.4	0.0215	0.0004
5	< 4		58	12			218	1	0.137	0.001
2	8	3	118	27	0.030	0.010	319	2	3.68	0.02
3	6	3	76	16	0.016	0.008	291	2	0.869	0.007
11	24	1	245	26	0.018	0.009	525	109	0.474	0.218

orresponds to the 1σ analytical error, which is based on reproducibility of the standards. F

This is a preprint, the final version is subject to change, of the American Mineralogist (MSA)
Cite as Authors (Year) Title. American Mineralogist, in press.
DOI: https://doi.org/10.2138/am-2019-6516

Comments
Surrounded by iron hydroxide Surrounded by iron hydroxide Surrounded by iron hydroxide Euhedral shape, possibly hydrothermal origin Grain has heterogeneous Pb abundances Grain has heterogeneous Pb abundances Mottled texture; next to serpentine vein Mottled texture; next to serpentine vein Mottled texture Mottled texture Part of grain with mottled texture Mottled texture Mottled texture Surrounded by iron hydroxide; heterogeneous Pb Grain has heterogeneous Pb abundances
Surrounded by iron hydroxide Surrounded by iron hydroxide Surrounded by iron hydroxide Surrounded by carbonate; heterogeneous Pb Contains some Cu; heterogeneous Pb Small grain (<50 µm diameter) Small grain (<50 µm diameter) Small grain (<50 µm diameter) Small grain (<50 µm diameter) Small grain (<50 µm diameter) Small grain (<50 µm diameter)
Grain has heterogeneous Pb abundances Grain has heterogeneous Pb abundances Grain has heterogeneous Pb abundances

'or grains with multiple analyses, the elements Pb,

This is a preprint, the final version is subject to change, of the American Mineralogist (MSA)
Cite as Authors (Year) Title. American Mineralogist, in press.
DOI: https://doi.org/10.2138/am-2019-6516

Figure 1

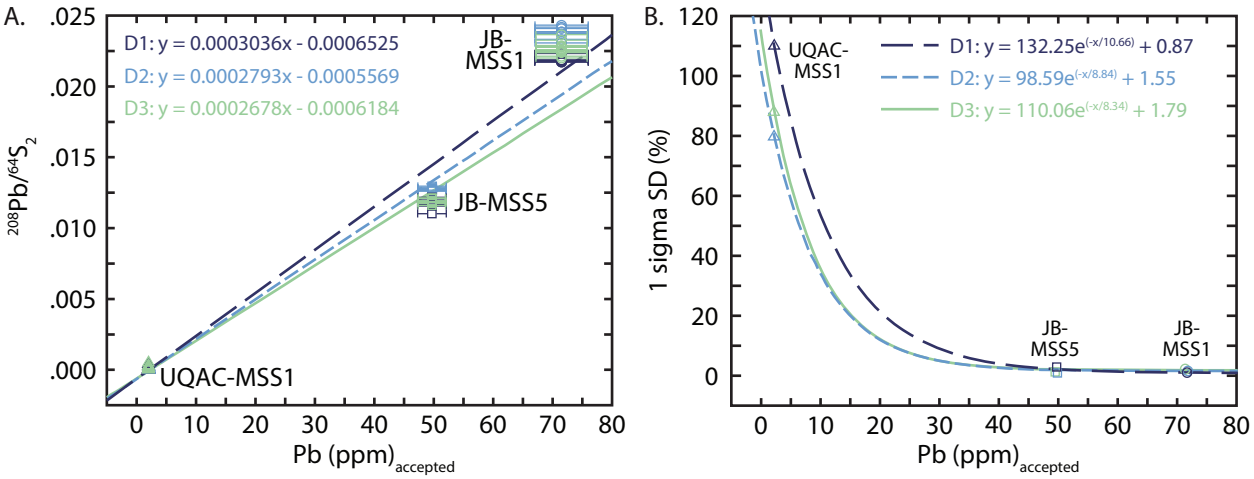

This is a preprint, the final version is subject to change, of the American Mineralogist (MSA)
Cite as Authors (Year) Title. American Mineralogist, in press.
DOI: https://doi.org/10.2138/am-2019-6516

Figure 2

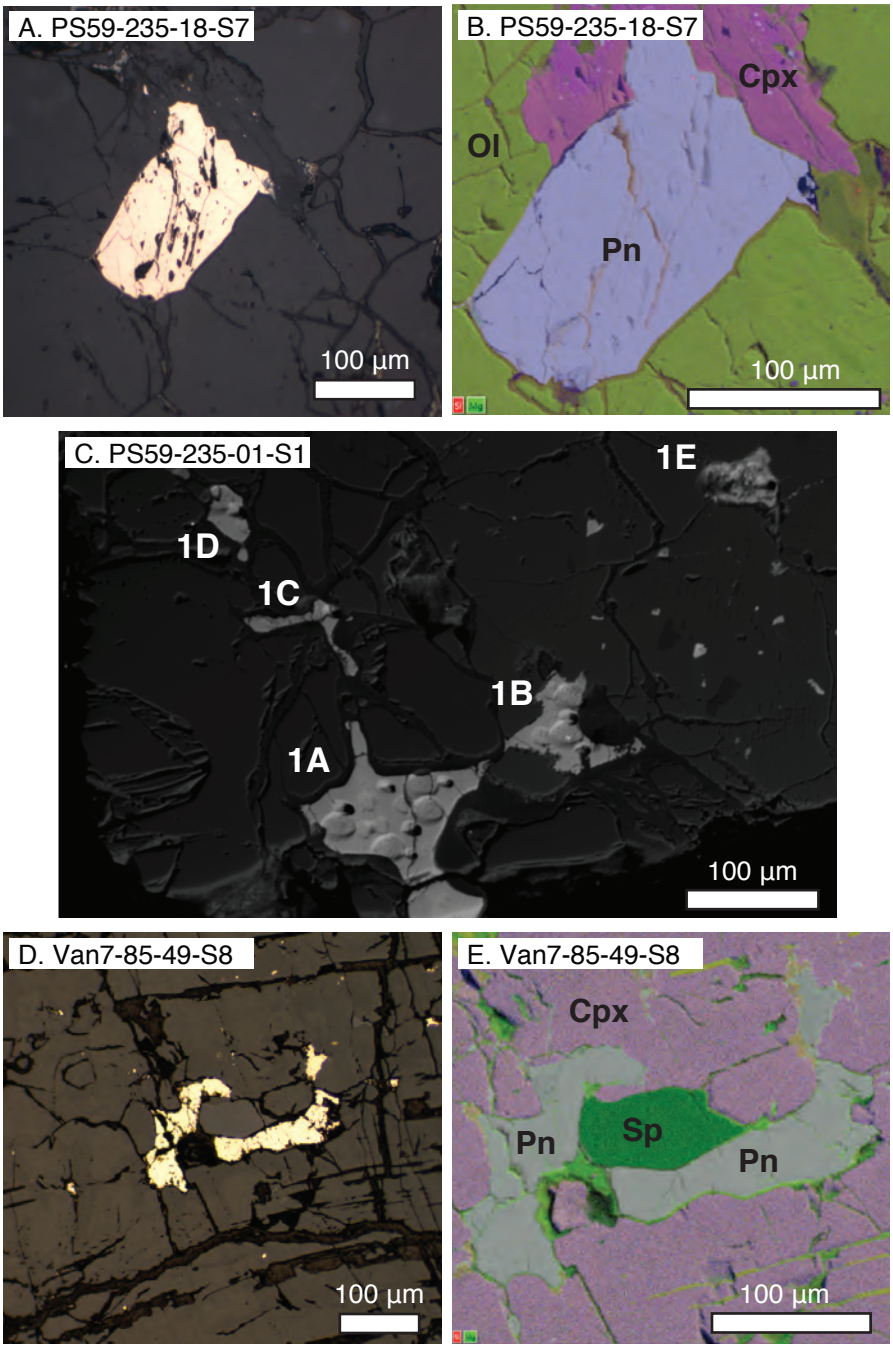

This is a preprint, the final version is subject to change, of the American Mineralogist (MSA)
Cite as Authors (Year) Title. American Mineralogist, in press.
DOI: https://doi.org/10.2138/am-2019-6516

Figure 3

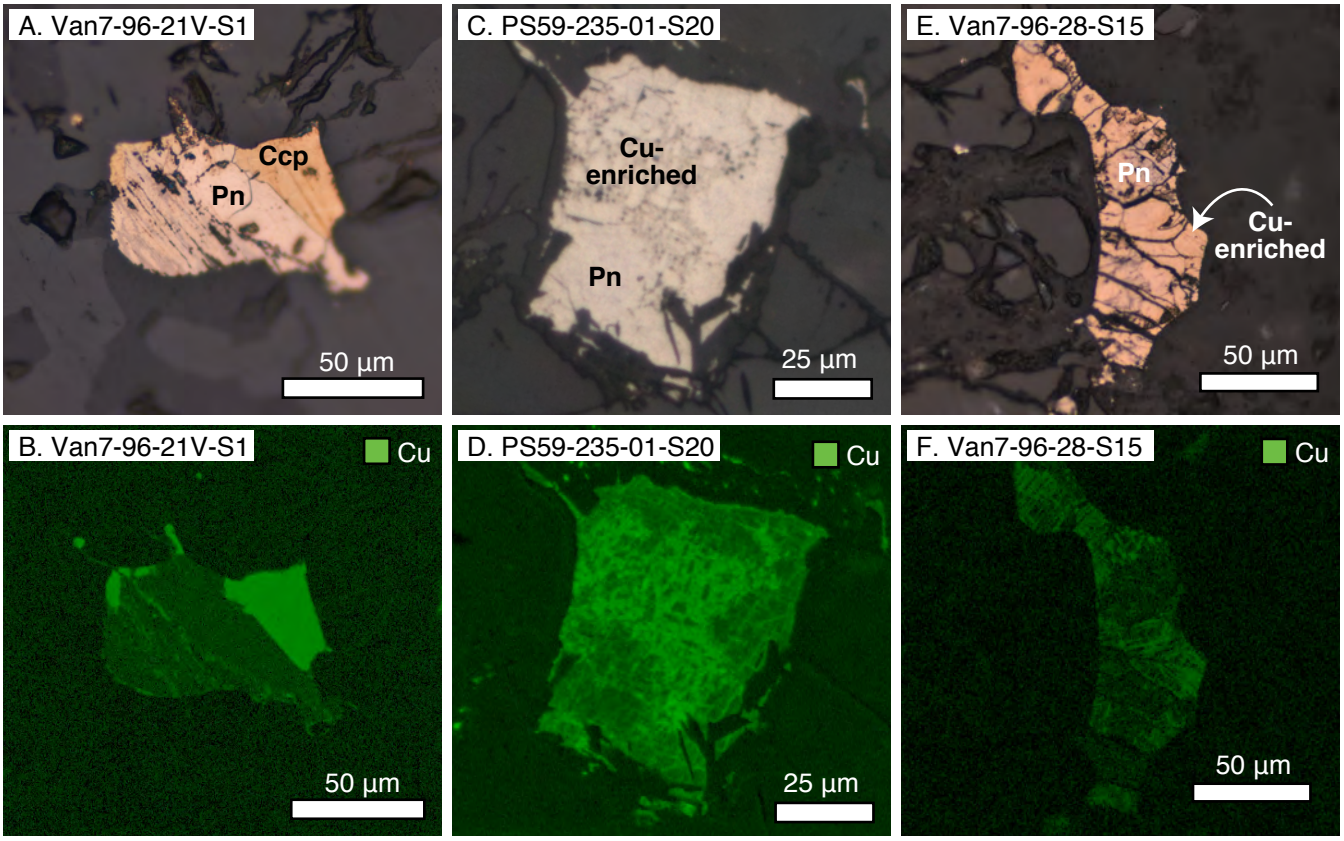

This is a preprint, the final version is subject to change, of the American Mineralogist (MSA)
Cite as Authors (Year) Title. American Mineralogist, in press.
DOI: https://doi.org/10.2138/am-2019-6516

Figure 4

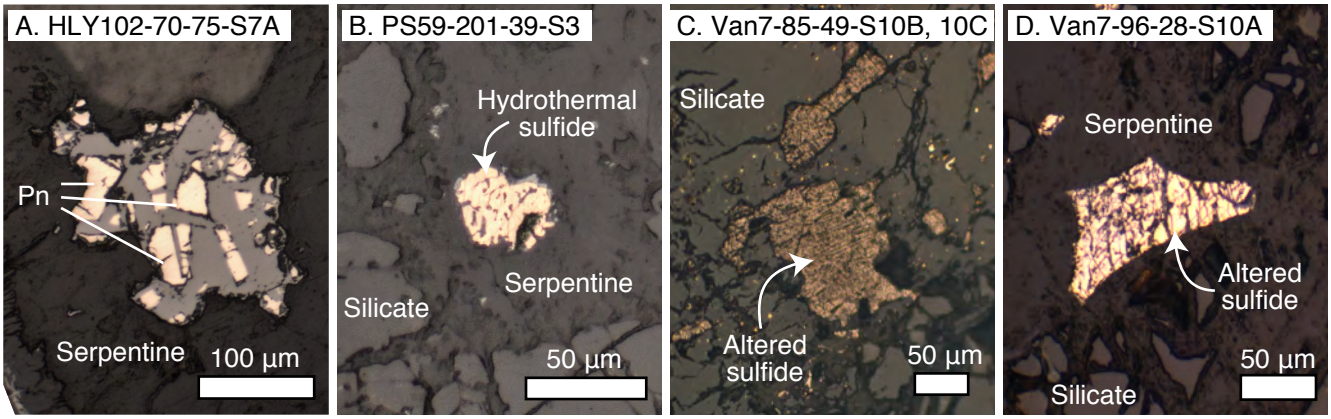

This is a preprint, the final version is subject to change, of the American Mineralogist (MSA)
Cite as Authors (Year) Title. American Mineralogist, in press.
DOI: https://doi.org/10.2138/am-2019-6516

Figure 5

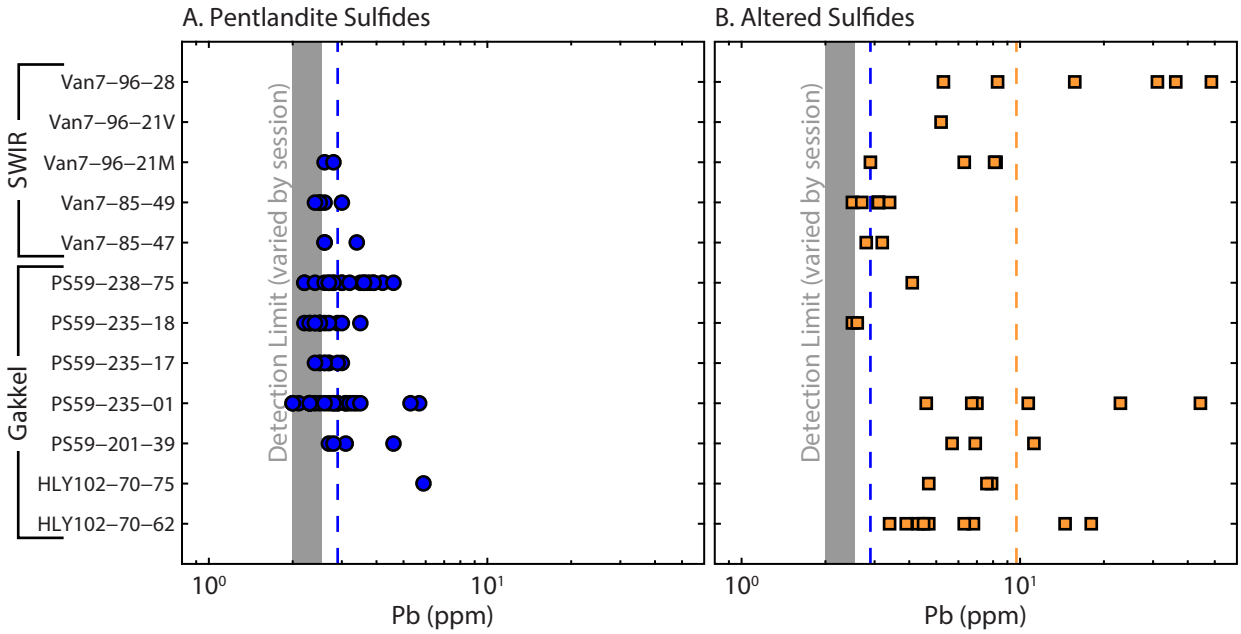

This is a preprint, the final version is subject to change, of the American Mineralogist (MSA)
Cite as Authors (Year) Title. American Mineralogist, in press.
DOI: https://doi.org/10.2138/am-2019-6516

Figure 6

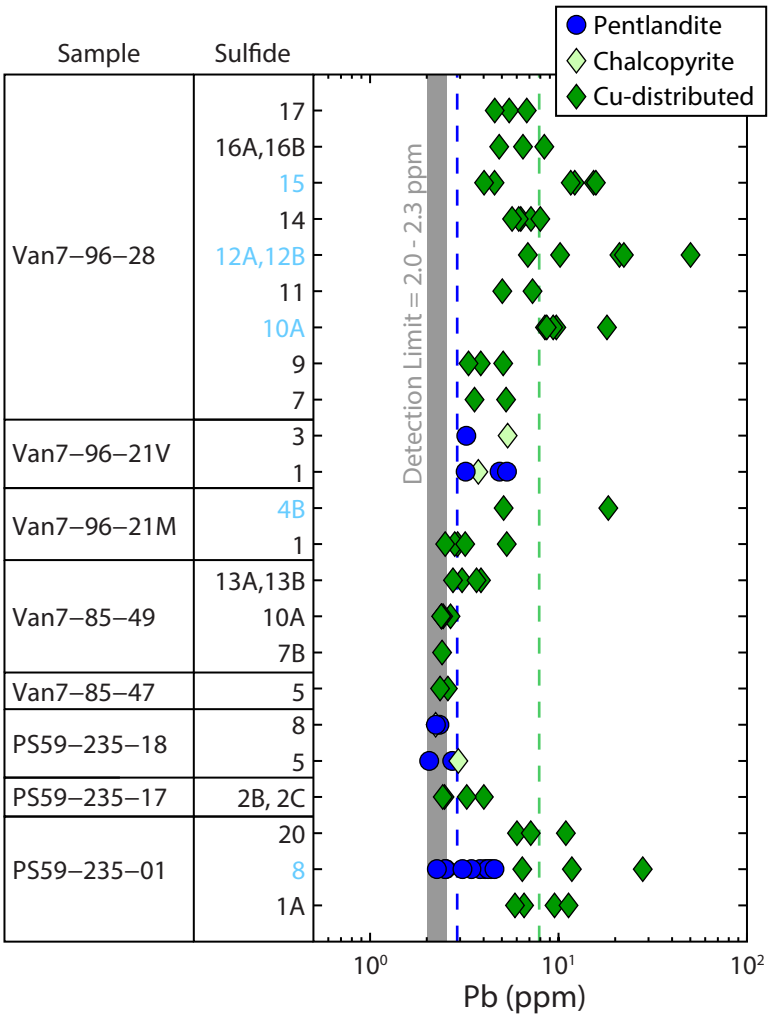

This is a preprint, the final version is subject to change, of the American Mineralogist (MSA)
Cite as Authors (Year) Title. American Mineralogist, in press.
DOI: https://doi.org/10.2138/am-2019-6516

Figure 7

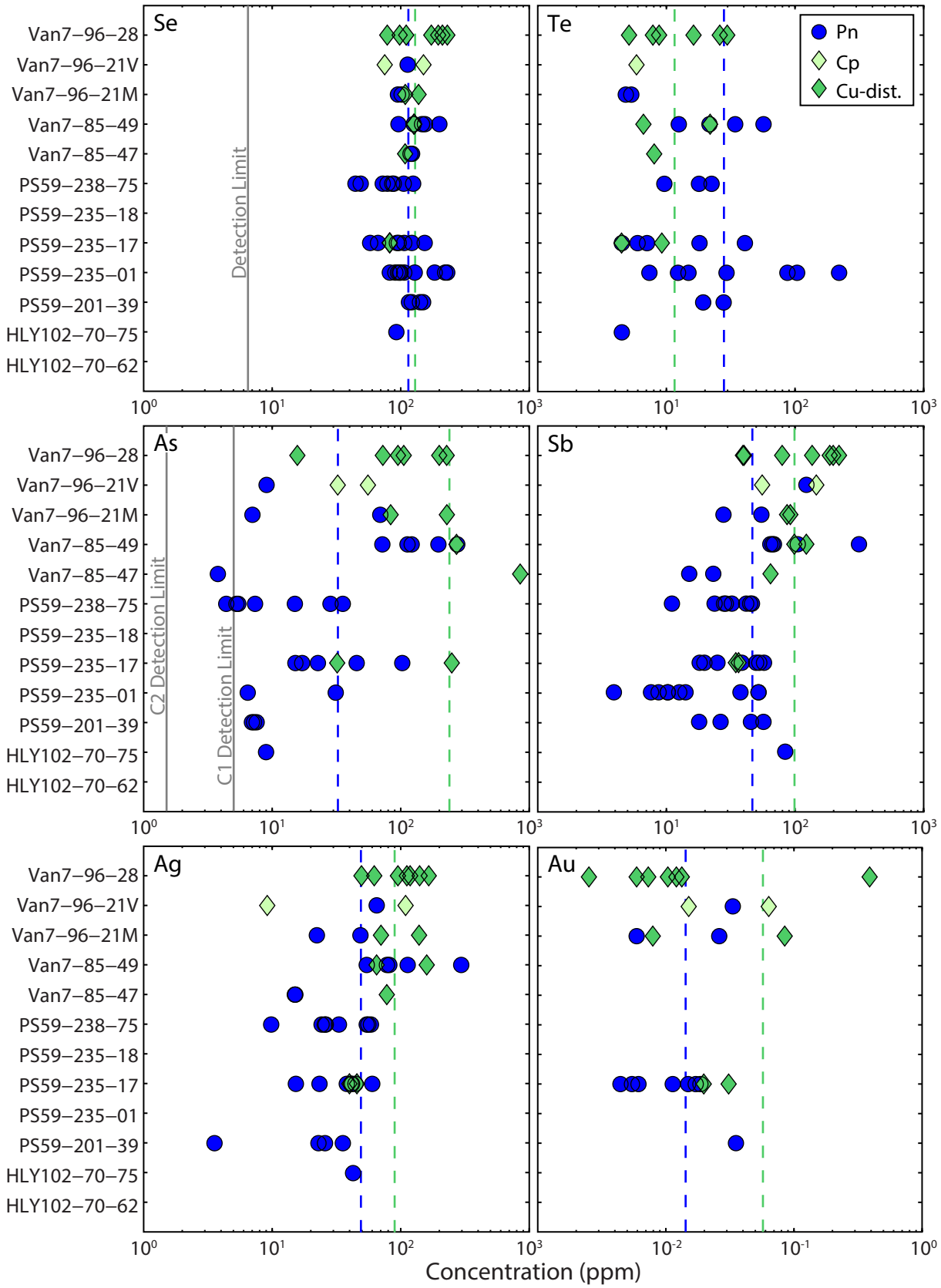

This is a preprint, the final version is subject to change, of the American Mineralogist (MSA)
Cite as Authors (Year) Title. American Mineralogist, in press.
DOI: https://doi.org/10.2138/am-2019-6516

Figure 8

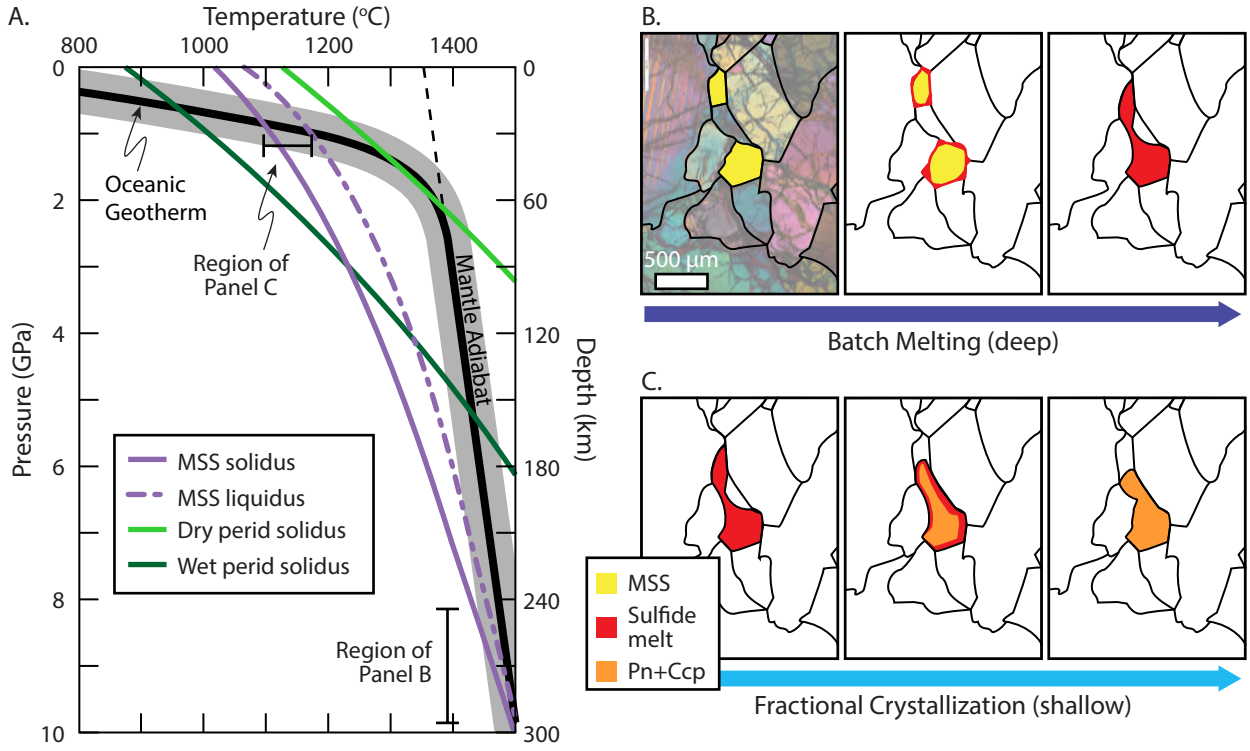

This is a preprint, the final version is subject to change, of the American Mineralogist (MSA)
Cite as Authors (Year) Title. American Mineralogist, in press.
DOI: https://doi.org/10.2138/am-2019-6516

Figure 9

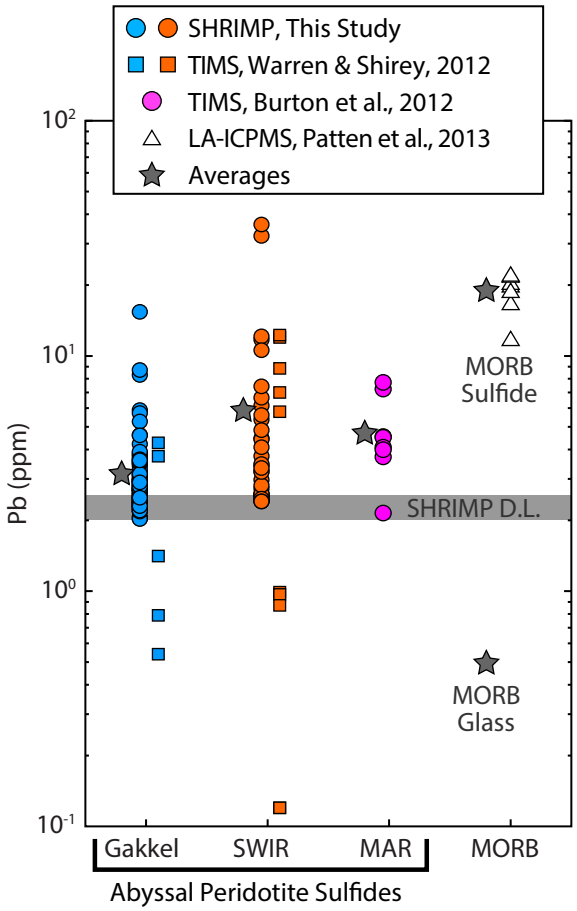

This is a preprint, the final version is subject to change, of the American Mineralogist (MSA)
Cite as Authors (Year) Title. American Mineralogist, in press.
DOI: https://doi.org/10.2138/am-2019-6516

Figure 10

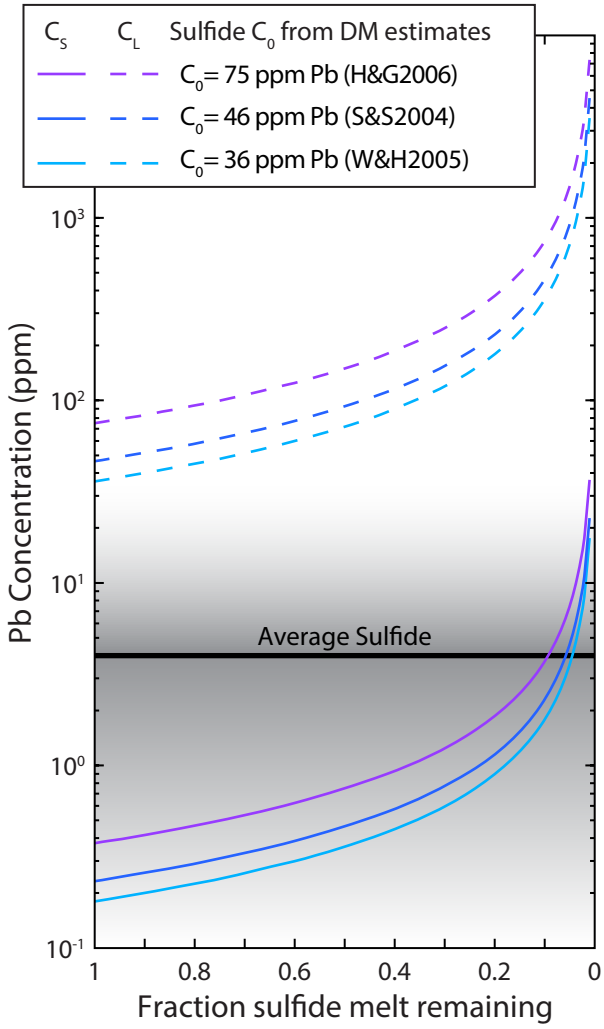

This is a preprint, the final version is subject to change, of the American Mineralogist (MSA)
Cite as Authors (Year) Title. American Mineralogist, in press.
DOI: https://doi.org/10.2138/am-2019-6516

Figure 11